

A STUDY OF HELIUM BUBBLE FORMATION BY SINGLE AND DUAL ION  
IMPLANTATION

A Thesis

by

JOSEPH ROBERT SACKMAN

Submitted to the Office of Graduate and Professional Studies of  
Texas A&M University  
in partial fulfillment of the requirements for the degree of  
MASTER OF SCIENCE

Chair of Committee, Lin Shao  
Committee Members, Pavel Tsvetkov  
Xiaofeng Qian  
Head of Department, John E. Hurtado

August 2019

Major Subject: Nuclear Engineering

Copyright 2019 Joseph Robert Sackman

## ABSTRACT

Helium bubble formation in materials is a concern for both modern day nuclear reactors as well as the next generation. Helium trapped in an atomic lattice has a tendency to form bubbles that may cause blisters, flaking, and increased porosity on the surface of a material. For this experiment a 10 kV linear accelerator was rebuilt and joined with a 1.7 MV linear accelerator to create a system where multiple ion species could be implanted in a sample material simultaneously. This dual ion beam system was used to examine the development of helium bubbles in stainless steel under both helium only implantation and helium with simultaneous implantation of a heavier ion species. It was observed in both a  $5.0 \cdot 10^{15}$  and  $3.0 \cdot 10^{16}$  ions $\cdot$ cm $^{-2}$  implantation that the additional damage from a second iron ion caused an increase in helium bubble nucleation across the entire range of 10 keV He $^{+}$  in a 316L stainless steel target.

## DEDICATION

To my best friend, wife, and editor in chief Rachel Sackman.

We made it.

## ACKNOWLEDGMENTS

I would like to thank the Texas A&M University Department of Nuclear Engineering for use of their facilities and resources to complete this thesis and my committee members Dr. Lin Shao, Dr. Pavel Tsevtkov, and Dr. Xiaofeng Qian for their support and guidance through this process. Special thanks to Dr. Wayne Kinneson, Dr. Jonathan Gigax, and Dr. Xumei Wang for their advice and mentoring throughout the last four years.

I would also like to thank my colleagues Andres Pacheco and Adam Gabriel for their aid in sample preparation and accelerator operation. Thanks to Dr. Jiangyuan Fan, Dr. Hyosim Kim, and Tianyao Wang for teaching me about the FIB and TEM processes and helping with the thermal study. Thanks to Ian Hemming of Highland Plastics Inc. and Dr. Erik Wahlin of Beam Imaging Systems for their their advice and donated materials used in the reconstruction of the accelerator.

Finally, I would like to thank Dr. Lin Shao. Four years ago he took me on as a student worker giving the opportunity and encouragement to prove I could do more. I owe him my deepest debt of gratitude.

## CONTRIBUTORS AND FUNDING SOURCES

### **Contributors**

This work was supported by a thesis committee consisting of Dr. Lin Shao and Dr. Pavel Tsvetkov of the Department of Nuclear Engineering and Dr. Xiaofeng Qian of the Department of Material Science & Engineering.

Raw materials used in construction were supplied by the Department of Nuclear Engineering or donated by Highland Plastics Inc. or Beam Imaging Systems.

Operation of the 10 kV and 1.7 MV accelerators was performed with aid from Adam Gabriel. Sample preparation was done in part by Andres Morel Pacheco. FIB sample preparation and TEM imaging was completed by Dr. Hyosim Kim and Tianyao Wang. The temperature study was modeled by Dr. Jiangyuan Fan in ANSYS.

All other work conducted for the thesis completed by the student independently.

### **Funding Sources**

No outside funding was received for the research and compilation of this document.

## NOMENCLATURE

BNC	Bayonet Neill Concelmann connector
DC	Direct current voltage
DD	Deuterium + Deuterium fusion
DPDT	Double-Pole Double-Throw switch
DT	Deuterium + Tritium fusion
LINAC	Linear particle accelerator
NAGDIS-II	Nagoya Diverter Simulator
SEM	Scanning Electron Microscope
SNICS	Source of Negative Ions by Cesium Sputtering
TEM	Transmission Electron Microscope
TFTR	Tokamak Fusion Test Reactor
TOKAMAK	Toroidal magnetic confinement fusion reactor
VAC	Alternating current voltage

# TABLE OF CONTENTS

	Page
ABSTRACT .....	ii
DEDICATION .....	iii
ACKNOWLEDGMENTS .....	iv
CONTRIBUTORS AND FUNDING SOURCES .....	v
NOMENCLATURE .....	vi
TABLE OF CONTENTS .....	vii
LIST OF FIGURES .....	ix
LIST OF TABLES.....	xii
1. INTRODUCTION AND THEORY .....	1
1.1 Problem Statement .....	1
1.2 Scope of Work.....	1
1.3 The Fusion Reaction .....	2
1.3.1 History & Development of Fusion Theory .....	3
1.3.2 Fusion Confinement .....	4
1.4 Bubble Nucleation and Helium Production .....	7
1.4.1 Vacancy Defects .....	7
1.4.2 Bubble Growth .....	9
1.4.3 Helium Sources .....	12
1.5 Previous Work .....	14
2. EXPERIMENTAL APPROACH .....	17
2.1 10 kV Accelerator Assembly .....	17
2.1.1 Lenses & Optics .....	18
2.1.2 Magnetic Bending .....	18
2.1.3 Beam Current Measurement .....	20
2.1.4 Electrical & Safety .....	21
2.1.5 Vacuum & Cooling Systems .....	22
2.1.6 System Alignment .....	23
2.2 1.7 MV Plasmatron/SNICS .....	25
2.2.1 Duoplasmatron Source .....	25

2.2.2	SNICS Source .....	28
2.2.3	Low Energy Filter Magnet .....	28
2.2.4	Acceleration Column .....	29
2.2.5	High Energy System .....	29
2.3	Target Chambers .....	31
2.4	Calibration Experiments .....	34
2.4.1	Ion Identification .....	34
2.4.2	Beam Uniformity .....	36
2.5	Mass Resolution .....	37
2.6	Helium Implantation in 316L Stainless Steel .....	41
2.6.1	Sample Preparation .....	41
2.6.2	Stage Preparation .....	41
2.7	Dual Implantation in 316L Stainless Steel .....	45
2.8	FIB Preparation and TEM Analysis .....	50
2.8.1	FIB Etching .....	50
2.8.2	TEM Imaging .....	56
2.8.3	Analysis in ImageJ .....	56
2.8.4	Bubble Concentration .....	58
3.	RESULTS AND DISCUSSION .....	59
3.1	Ion Identification .....	59
3.2	10 keV He <sup>+</sup> into Stainless Steel .....	63
3.3	He vs. Fe+He Implantation .....	65
3.3.1	Deposition of He Across Samples .....	65
3.3.2	5·10 <sup>15</sup> Φ Irradiation of 316L .....	68
3.3.3	3·10 <sup>16</sup> Φ Irradiation of 316L .....	72
3.3.4	Temperature Study .....	75
4.	CONCLUSION .....	77
	REFERENCES .....	78
	APPENDIX A. DATA .....	80
	APPENDIX B. SCHEMATICS .....	81
	APPENDIX C. PYTHON CODE .....	86



## LIST OF FIGURES

FIGURE	Page
1.1 Binding energy by mass number . Reprinted from <i>Lépine-Szily 2012</i> [1]. . . . .	3
1.2 Circular path of charged particles in magnetic field B . Reprinted from <i>Miyamoto 2005</i> [2]. . . . .	5
1.3 Cutaway schematic of a Tokamak fusion reactor . Reprinted from <i>Li 2014</i> [3]. . . . .	6
1.4 Single vacancy in an atomic lattice. . . . .	7
1.5 Single vacancy and displacement. . . . .	9
1.6 Helium trapped in lattice void. . . . .	10
1.7 Trajectory of an $\alpha$ particle born in a banana orbit . Reprinted from <i>Darrow 1996</i> [4].	12
1.8 SEM images of 316L stainless steel after a) 70 keV He <sup>+</sup> implantation and b) subsequent annealing at 700 K . Reprinted from <i>Wang 1989</i> [5]. . . . .	14
1.9 Cross-sectional SEM images of W targets exposed to pure He plasma in the PISCES-B for (a) 300 s, (b) $2.0 \cdot 10^3$ s ,(c) $4.3 \cdot 10^3$ s, (d) $9.0 \cdot 10^3$ s, (e) $2.2 \cdot 10^4$ s. $\Gamma_{\text{He}^+}=(4-6) \cdot 10^{22} \text{ m}^{-1} \text{ s}^{-1}$ . Reprinted from <i>Baldwin and Doerner 2008</i> [6]. . . . .	15
1.10 Surface porosity from 1 to 30 eV helium implanted on powder metallurgy tungsten in the NAGDIS-II. Reprinted from <i>Nishijima 2004</i> [7]. . . . .	16
1.11 Tungsten morphology after H+C+He irradiation at 1 keV . Reprinted from <i>Ueda 2009</i> [8]. . . . .	16
2.1 Colutron DC ion source schematic. . . . .	17
2.2 Schematic of beam focusing via an einzel lens. . . . .	18
2.3 Path of various 10 keV ions through a 0.4 m, 283 Gauss field. . . . .	19
2.4 Typical hysteresis curve in a solid core electromagnet. . . . .	20
2.5 Schematic of the collection plate selection switch and current integrator. . . . .	20
2.6 Front (a) and side (b) view of the steel slits used to define the beam shape. . . . .	21
2.7 Self-latching relay system for an emergency shutdown of the accelerator. . . . .	22

2.8	Vertical laser alignment. ....	24
2.9	Horizontal laser alignment. ....	24
2.10	Duoplasmatron source diagram. ....	26
2.11	SNICS source diagram. ....	27
2.12	Tandem acceleration column diagram. ....	30
2.13	Target chamber geometry, top down view. ....	32
2.14	Multibeam chamber geometry, top down view. ....	33
2.15	Magnetic field for a given ion to bend at a 1.016 m radius at 10 keV. ....	35
2.16	Beam paths with tangent trajectories. ....	37
2.17	Geometry of beam path. ....	38
2.18	$\theta$ as a function of $R_{m,q}$ . ....	40
2.19	Burned paper marking beam spot ....	43
2.20	316L sample mounted to Inconel hot stage. ....	44
2.21	Overlapped Fe and He beam spots. ....	46
2.22	Overlapping beam spot measurements. ....	47
2.23	Pattern of irradiation across dual beam samples. ....	48
2.24	Platinum buildup on sample surface. ....	51
2.25	Troughs cut to form thin lamella for TEM imaging. ....	52
2.26	J-cut made into lamella for lift out procedure. ....	53
2.27	Lamella welded to probe with platinum and cut from bulk sample. ....	54
2.28	Lamella welded to TEM grid ready for imaging. ....	55
2.29	97kx resolution of He+Fe lamella. ....	56
2.30	97kx TEM image of 3E16 He implantation. ....	57
2.31	Sample image a) before and b) after bubble marking and measurement. ....	58
3.1	$H^+, He^{2+}(D), He^+, Li^+, N^+(CO^{2+}), CO_2^{+,2+}$ . ....	60

3.2	B-I curve for $H^+, He^{2+}(D), He^+, Li^+, Na^+, Ca^+$ .....	61
3.3	B-I curve for $H^+, He^{2+}(D), He^+, Li^+, Fe^{+,2+}$ .....	62
3.4	Stainless steel after $8 \cdot 10^{16}$ ions $\cdot$ cm $^{-2}$ $He^+$ dose. ....	63
3.5	97kx magnification of stainless steel after $8 \cdot 10^{16}$ ions $\cdot$ cm $^{-2}$ $He^+$ dose. ....	64
3.6	Total volume of helium by depth for $5.0 \cdot 10^{15}$ ions $\cdot$ cm $^{-2}$ . ....	66
3.7	Total volume of helium by depth for $3.0 \cdot 10^{16}$ ions $\cdot$ cm $^{-2}$ . ....	67
3.8	Bubble radius by depth for $5.0 \cdot 10^{15}$ ions $\cdot$ cm $^{-2}$ He. ....	68
3.9	Bubble radius by depth for $5.0 \cdot 10^{15}$ ions $\cdot$ cm $^{-2}$ He+Fe.....	69
3.10	Average bubble formation size for $5.0 \cdot 10^{15}$ ions $\cdot$ cm $^{-2}$ He & He+Fe.....	70
3.11	Bubble concentration by depth for $5.0 \cdot 10^{15}$ ions $\cdot$ cm $^{-2}$ He & He+Fe.....	71
3.12	Bubble radius by depth for $3.0 \cdot 10^{16}$ ions $\cdot$ cm $^{-2}$ He. ....	72
3.13	Bubble radius by depth for $3.0 \cdot 10^{16}$ ions $\cdot$ cm $^{-2}$ He+Fe.....	73
3.14	Average bubble formation size for $3.0 \cdot 10^{16}$ ions $\cdot$ cm $^{-2}$ He & He+Fe.....	74
3.15	Bubble concentration by depth for $3.0 \cdot 10^{16}$ ions $\cdot$ cm $^{-2}$ He & He+Fe.....	75
3.16	ANSYS thermal study of surface temperature distribution.....	76
B.1	Colutron DC ion source schematic. Adapted from <i>Wahlin 2018</i> [9].....	81
B.2	Electrical input flange schematics. ....	82
B.3	Colutron 200-B lens system, dimensions in inches. Adapted from <i>Wahlin 2018</i> [9]. ..	83
B.4	10 keV Beamline schematic. ....	84
B.5	Bending magnet dimensions and properties. Adapted from <i>HVE 2018</i> [20]. ....	85

## LIST OF TABLES

TABLE	Page
2.1 Fluences and temperatures for dual beam implantations. ....	49
3.1 Results of magnet scans. ....	59
A.1 Magnetic fields required for ions bending at a 1.016 m radius. ....	80

# 1. INTRODUCTION AND THEORY

## 1.1 Problem Statement

Fusion technology represents the next generation of nuclear reactors and ion propulsion devices. As such the need for materials capable of withstanding interaction with a fusion plasma for long periods of time is high.  $^4\text{He}$  ions are a concern in any fusion or plasma equipment as they have a tendency to create bubbles within the atomic lattice during irradiation. This process can lead to accelerated swelling, corrosion, and cracking of shielding materials. Examining how this damage occurs under fusion-like conditions will aid in materials development for next generation plasma facing materials.

## 1.2 Scope of Work

The scope of this thesis was to construct an accelerator system capable of simultaneous ion implantation to simulate surface helium implantation into a plasma facing material from a confined fusion plasma. Two linear accelerators were used to simulate the release of ions in the plasma. A 10 kV DC ion source was constructed to simulate the bombardment of thermalized ions and a 1.7 MV Plasmatron/SNICS source to simulate higher energy ions.

Linear accelerators were chosen for use in this experiment for three main reasons: they allow for variation in displacement per atom (dpa) through variable gas loading, are capable of producing the same fluence as a reactor at a fraction of the cost and time, and allow multiple separate samples to be irradiated simultaneously under the same operating conditions. The use of two independent beam lines in this design allow multiple ion species to interact with a single target to more closely resemble the conditions in a fusion-like plasma.

### 1.3 The Fusion Reaction

Nuclear fusion occurs when two atoms are able to overcome the electrostatic force  $F_c$  between them and allow the nuclear force to bind them into a new isotope. This force is described in Equation 1.1.

$$F_c = \frac{Z_x Z_X e^2}{4\pi\epsilon_o r^2} \quad (1.1)$$

Where  $Z_x$  and  $Z_X$  are the number of protons in atoms  $x$  and  $X$  respectively,  $r$  is the distance between the atoms in meters,  $\epsilon_o$  is the permittivity of free space, and  $e$  is the elemental charge  $1.6 \cdot 10^{-19}$  C. The energy  $E_{fusion}$  required to overcome the force is:

$$E_{fusion} = W = \frac{Z_x Z_X e^2}{4\pi\epsilon_o r} \quad (1.2)$$

The energy released by such a fusion is calculable with thanks to Einstein's famous mass-energy equivalence  $E = mc^2$  and a careful measurement of the mass defect  $\Delta M$  in a reaction:

$$\Delta M = \sum m_{reactants} - \sum m_{products} \quad (1.3)$$

When  $\Delta M$  is calculated in amu it can be converted directly to a quantity of energy by multiplying it by  $c^2$ :

$$Q_{rxn} = \Delta M c^2 = \Delta M \left( 931.5 \frac{\text{MeV}}{\text{amu}} \right) \quad (1.4)$$

When lighter elements are fused together the reaction becomes exothermic, as in the case of  ${}^7\text{Li}$  fusing with a proton:



This reaction results in a  $\Delta M$  of  $1.866 \cdot 10^{-2}$  amu, or  $\approx 17.4$  MeV [10]. Figure 1.1 illustrates the binding energy per nucleon and the limits of fusion and fission by mass number. Fusion of heavier elements up to  ${}^{56}\text{Fe}$  are possible. The energy required to fuse nuclides heavier than  ${}^{56}\text{Fe}$  is simply too large to occur in nature or any known technology.

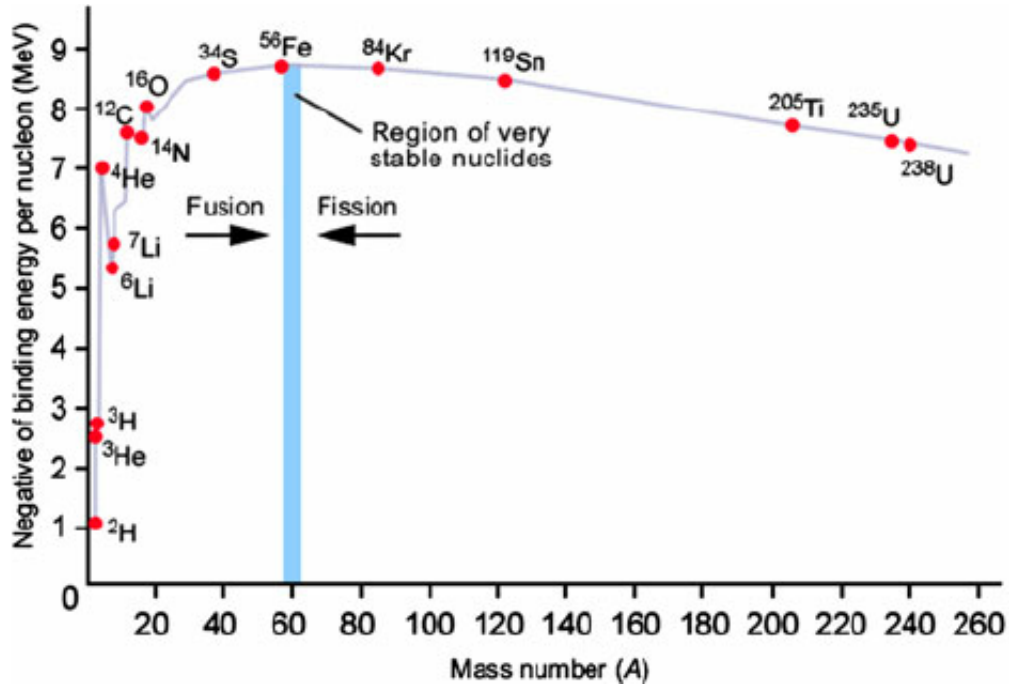
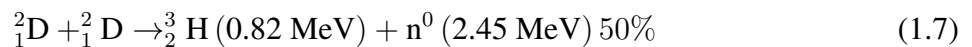
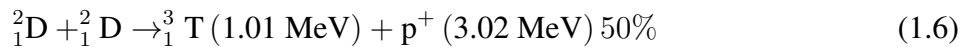
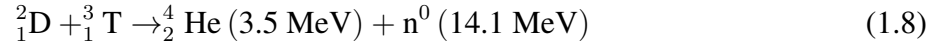


Figure 1.1: Binding energy by mass number . Reprinted from *Lépine-Szily 2012*[1].

### 1.3.1 History & Development of Fusion Theory

Nuclear fusion was first proposed as the source of stellar energy by Arthur Eddington in 1929. The proof of the stellar proton-proton chain reaction was developed by Hans Bethe in 1938 and would eventually earn him the Nobel Prize in 1967. The first successful laboratory fusion was carried out by Mark Oliphant, Ernest Rutherford, and Paul Harteck in 1939. This initial fusion was achieved by using a particle accelerator to fire deuterium ions into a thin foil that had been prepared with a solution containing deuterium atoms [11]. In this process Oliphant et al discovered the release of a high energy helium atom, the new hydrogen isotope tritium, a proton, and neutron. The DD fusion reaction and products can be seen in Equations 1.1 and 1.2 respectively [12].





Deuterium is a commonly occurring natural isotope of hydrogen, making DD a cost effective fusion from a materials standpoint. DT fusion (Equation 1.8) however has the lowest energetic threshold for fusion reactions making it more cost effective from an energy consumption standpoint [13].

### 1.3.2 Fusion Confinement

Fusion confinement is currently achieved with two methods: an inertial method that simulates the pressure from gravity via laser bombardment and magnetic confinement that traps ions in a helical path. Magnetic confinement utilizes the conductive nature of plasma to contain ions in a helical path. Ions passing through a magnetic field are subjected to the Lorentz Force Law:

$$\vec{F} = q\vec{v} \times \vec{B} \quad (1.9)$$

This centripetal force results in a circular ion path as illustrated in Figure 1.2 where the Larmor radius  $\rho_\Omega$  is dictated by the strength of the magnetic field  $B$  and the charge and momentum of the particle in the field. Magnetic confinement can be found in Tokamak and pinch devices. The Tokamak uses a toroidal enclosure as seen in Figure 1.3 to wind the path of ions back onto themselves while forcing them to overcome the Coloumb barrier and fuse into heavier elements.



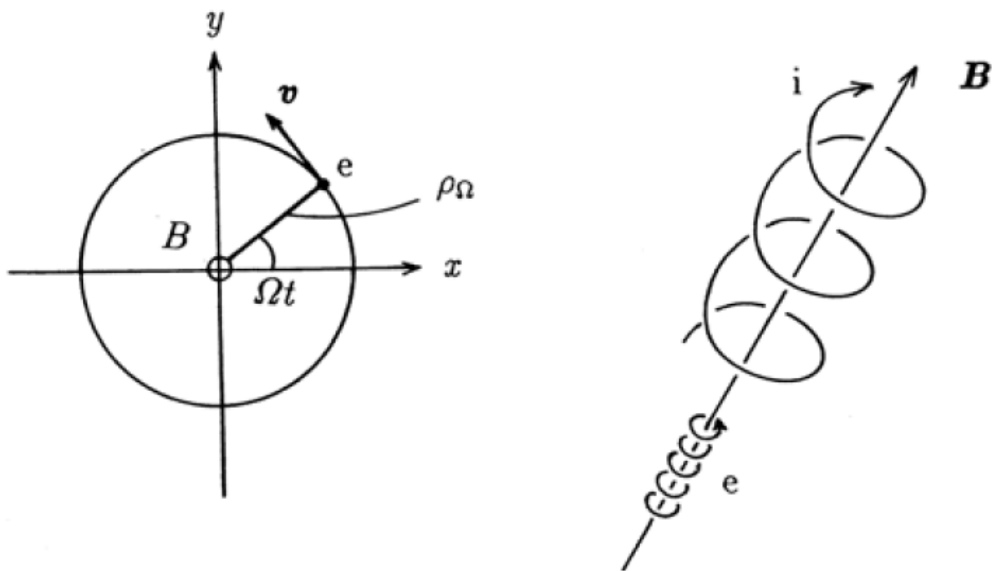


Figure 1.2: Circular path of charged particles in magnetic field  $B$  . Reprinted from *Miyamoto 2005* [2].

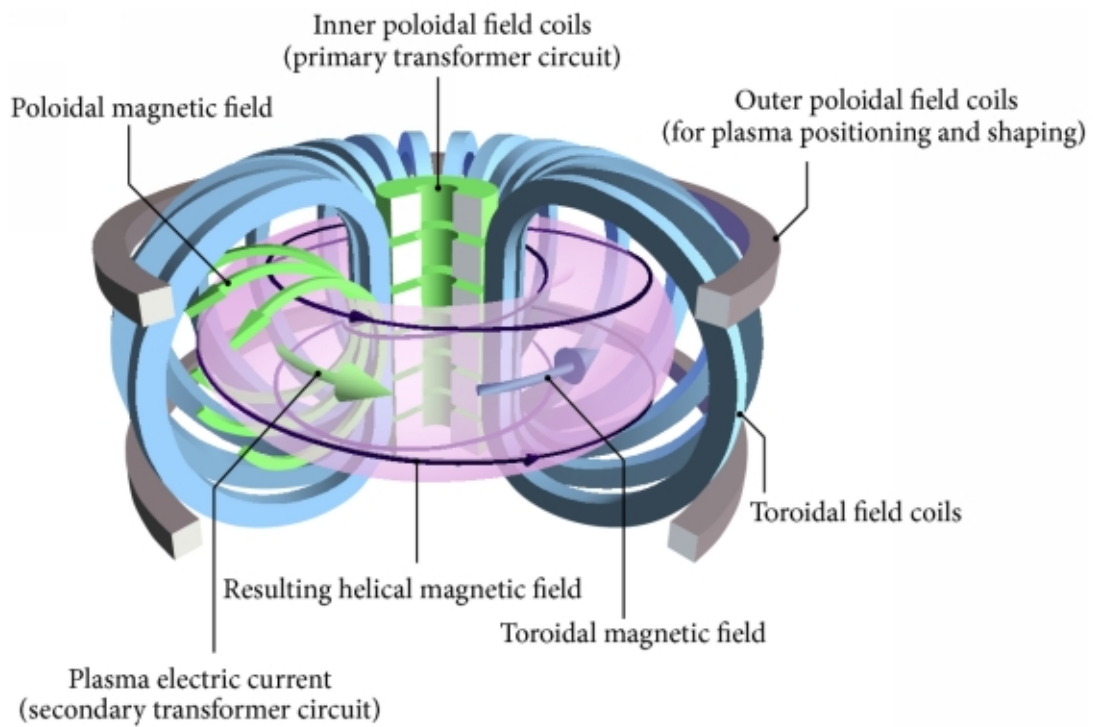


Figure 1.3: Cutaway schematic of a Tokamak fusion reactor . Reprinted from *Li 2014*[3].

## 1.4 Bubble Nucleation and Helium Production

### 1.4.1 Vacancy Defects

Helium bubble nucleation first begins in vacancy point defects within the atomic structure of a material. Vacancies in a material are due to atoms missing within the atomic lattice as seen in Figure 1.4.

The number of equilibrium vacancies  $N_v$  in a given material is dependent on the energy  $Q_v$  required to form a vacancy and the temperature  $T$  of the material according to the relationship:

$$N_v = N e^{-\frac{Q_v}{kT}} \quad (1.10)$$

where  $N$  is the total number of atoms present and  $k$  is Boltzmann's constant which can be expressed as either  $1.38 \cdot 10^{-23} \text{ J} \cdot \text{atoms}^{-1} \cdot \text{K}^{-1}$  or  $8.62 \cdot 10^{-23} \text{ eV} \cdot \text{atoms}^{-1} \cdot \text{K}^{-1}$  depending on the units of  $Q_v$ .

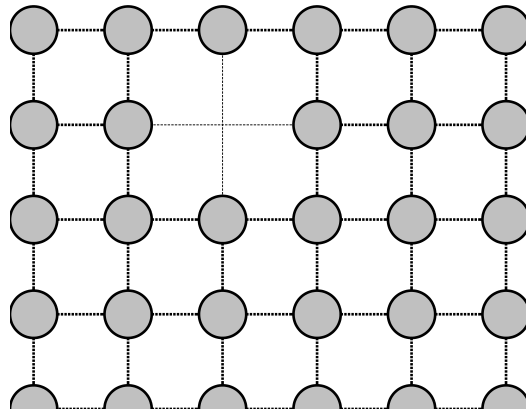


Figure 1.4: Single vacancy in an atomic lattice.

From Equation 1.9 it can be seen that as temperature in a material is increased the number of vacancies exponentially increases.

These vacancies are also formed from interactions between the target ions, neutrons or other energetic particles released from nuclear reactions or radioactive decays. In neutron-nucleus col-

lisions energy is imparted to the primary knock on-atom (PKA) when a scattering event occurs. This transferred energy  $E_{PKA}$  is determined by the mass of the PKA  $M$  and incident neutron  $m$ . In a completely elastic scattering event  $E_{PKA}$  is calculated by:

$$E_{PKA} = \frac{2M}{(M+1)^2} E_i (1 - \cos(\phi)) \quad (1.11)$$

where  $E_i$  is the incident neutron energy and  $\phi$  is the recoil scattering angle between the neutron and nucleus. Assuming an isotropic scattering angle for elastic collisions will yield:

$$\bar{E}_{PKA} = \frac{2M}{(M+1)^2} E_i \quad (1.12)$$

Elastic scattering assumes that kinetic energy is perfectly preserved in the collision. PKAs can also undergo inelastic scattering where a portion of kinetic energy is lost and the PKA is left in an excited state post-collision. For a given  $\gamma$  decay with energy  $Q_j$ , an incident neutron of energy  $E_i$ :

$$E_{PKA} = \beta E_i - \beta [E_i (E_i + Q_j \frac{M+1}{M})]^{\frac{1}{2}} \cos(\phi) + \frac{Q_j}{M+1} \quad (1.13)$$

where:

$$\beta = \frac{2M}{(M+1)^2} \quad (1.14)$$

The average  $E_{PKA}$  in this situation is dependent on the resonance scattering cross-section of the material. The scattering cross section  $\sigma_{s,j}$  for a resolved resonance region can be calculated as:

$$\sigma_{s,j}(E_i, Q_j, E_{PKA}) = \frac{\sigma_{s,j}}{\beta E_i (1 - \frac{Q_j M+1}{E_i M})} \quad (1.15)$$

Ion-nucleus collisions are another potential source for vacancies. For a collision between two atoms of mass  $M_i$  and radius  $r_i$  the total transferable energy is:

$$E_{PKA} = \frac{M_1 M_2}{2(M_1 + M_2)} (\dot{r}^2 + r^2 \dot{\psi}^2) + V(r) \quad (1.16)$$

where  $\dot{\psi}$  and  $\dot{r}$  are the sums of the transverse and radial velocities of  $M_1$  and  $M_2$ .  $V(r)$  is the potential energy between  $M_1$  and  $M_2$  due to the Coulombic interaction between them. The simplest of this model is:

$$V(r) = \frac{Z_1 Z_2 \epsilon^2}{r} \quad (1.17)$$

Where  $Z_i$  is the atomic number of mass  $M_i$ ,  $r$  is the total distance between them, and  $\epsilon^2 = 1.44$  eV·nm [14]. Atoms can also be displaced through (n, $\gamma$ ) and (n,2n) reactions that occur after a neutron is absorbed by the PKA. In each case the PKA is left in an excited state and will emit either additional neutrons or  $\gamma$  and the recoil energy from the release will knock the PKA out of its lattice position.

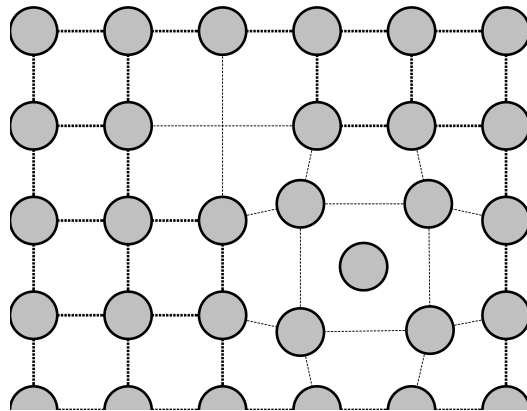


Figure 1.5: Single vacancy and displacement.

A displacement such as the one in Figure 1.5 occurs when enough energy is transmitted to the PKA for it to scatter out of its position in the lattice. These displaced atoms represent an additional source of vacancies as they often are energetic enough to knock a subsequent atom out of its lattice. Such damage cascades vastly increase the production of vacancies during a period of irradiation.

### 1.4.2 Bubble Growth

Bubbles begin to form in a solid as helium diffuses through the atomic lattice and become lodged in vacancy sites. As seen in Figure 1.6 multiple helium atoms become trapped within the

same vacancy they begin to exert gas pressure  $p$  on the surrounding lattice. The change in the free energy  $dG$  of the solid from a bubble of radius  $R$  is shown in Equation 1.18.

$$\frac{dG}{dr} = -4\pi R^2 \left( p - \frac{2Q_s}{R} \right) \quad (1.18)$$

Where  $Q_s$  is the surface energy surrounding the bubble. The equilibrium condition for such a bubble will occur when the gas pressure is equal to the inward stress from surface tension minus any additional surface tension  $\sigma$  applied as in Equation 1.19.

$$p = \frac{2Q_s}{R} - \sigma \quad (1.19)$$

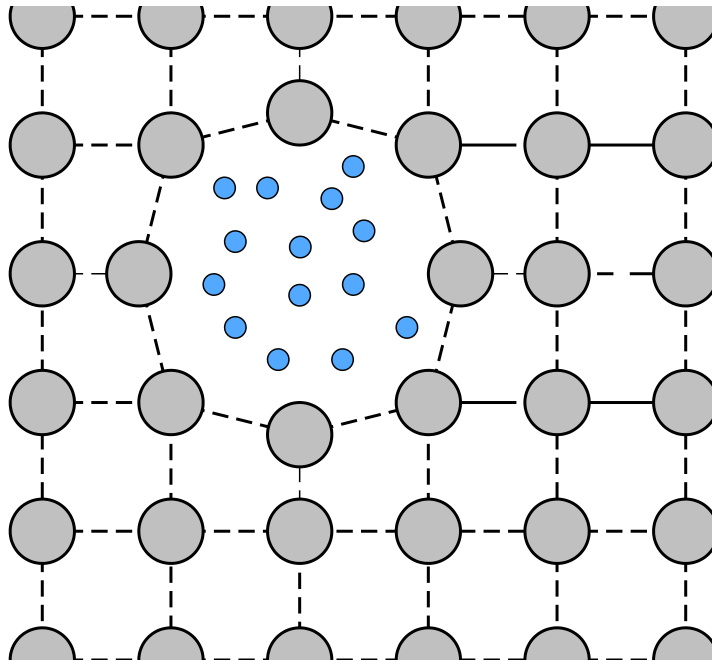


Figure 1.6: Helium trapped in lattice void.

By using the equilibrium condition and the ideal gas law the number of particles  $n_{He}$  in a

bubble of radius  $R$  can be calculated with Equation 1.20.

$$n_{He} = \frac{8\pi R^2 Q_s}{3kT} \quad (1.20)$$

Likewise, the number of vacancies  $n_v$  required for a bubble in mechanical equilibrium can be found by treating the bubble as an absence of atoms with volume  $V_{solid}$  by using Equation 1.21.

$$n_v = \frac{4\pi R^3}{3V_{solid}} \quad (1.21)$$

The critical radius  $R_c$  at which a bubble grow uninhibited is related to the equilibrium radius  $R$  by  $\sqrt{3}R_0$ . The critical applied stress  $\sigma_c$  that will induce bubble growth is:

$$\sigma_c = \frac{2Q_s}{R_c} \left(1 - \frac{R_0^2}{R_c^2}\right) \quad (1.22)$$

For bubbles  $R_0 < R_c$  when stress  $\sigma_c$  is applied the bubbles will grow to  $R_c$ . If  $R_0 > R_c$  or a stress greater than  $\sigma_c$  is applied the bubble will continue to grow uninhibited. As the number of gas particles within the bubble increases an increasing number of vacancies must also be introduced to maintain mechanical equilibrium. The growth rate of of bubbles is dictated by the concentration of vacancies and interstitial atoms in the bulk sample and their ability to travel within the medium [14]. This rate  $\dot{R}$  can be described as:

$$\dot{R} = \frac{V_{solid}}{R} [D_v(C_v - C_v^v) - D_i(C_i - C_i^v)] \quad (1.23)$$

$C_v^v$  and  $C_i^v$  in this equation are the vacancy and interstitial concentrations at the bubble surface and  $C_v$  and  $C_i$  are those same concentrations for the bulk solid.

### 1.4.3 Helium Sources

Helium can be generated in two ways within a fusion reactor. Either helium produced from reaction will be implanted into the surface of plasma facing materials, or the absorption of neutrons in target atoms will yield  $\alpha$  particles as a decay product. Research done with the Tokamak Fusion Test Reactor (TFTR) has been able to separate three distinct loss mechanisms within a toroidal fusion chamber. The first orbit loss stems from particles born on "banana" orbits shown in Figure 1.7 [4].

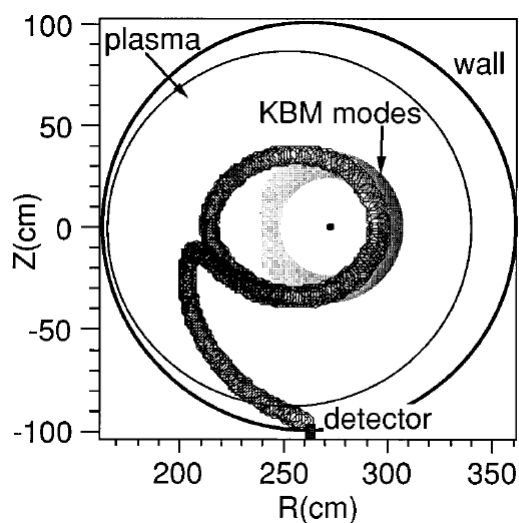


Figure 1.7: Trajectory of an  $\alpha$  particle born in a banana orbit . Reprinted from *Darrow 1996* [4].

RF wave-induced loss can occur in the plasma when the wave-particle resonance condition is satisfied in Equation 1.24.

$$\omega_{\text{RF}} = \Omega_f(R) - k_{\parallel} v_{\parallel f} \quad (1.24)$$

Where  $\omega_{\text{RF}}$  is the applied rf frequency,  $\Omega_f(R)$  is the fast ion cyclotron frequency,  $R$  is the major radial position,  $k_{\parallel}$  is the parallel wave number, and  $v_{\parallel f}$  is the fast ion parallel velocity. In this mode the ion cyclotron range of frequencies wave (ICRF) interact with fast particles to move them into

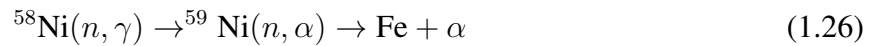


banana orbits and cause loss. Lastly, a collective instability known as the Toroidicity-induced Alfvén Eigenmode (TAE) has been observed to cause magnetic perturbations in the confinement field allowing particles to escape their orbit. The study performed by Darrow, Zweben, and Batha et. al. however did not account for any low energy  $\alpha$  particle observance as thin foils placed over the detectors acted as a shield for any  $\alpha$  below approximately 900 keV.

The neutrons emitted during the fusion reaction also have the potential to be absorbed by nuclei in the surrounding materials. These nuclei can then produce additional helium through a  $(n,\alpha)$  reaction scheme in Equation 1.25.



Transmutation can happen in a number of nuclides but the most prominent in a reactor environment is the two step reaction from  ${}^{58}\text{Ni}$ .



It is worth noting that this reaction is more likely to happen with neutrons in the thermal range. This reaction also carries with it additional damage cascades as the recoil from the  $\gamma$  released will carry the nickel atom out of its lattice position.

## 1.5 Previous Work

The surface effects of helium bubbles on metals has been examined in a number of studies. Helium deposition has been shown to cause increased bubbling and flaking on metallic surfaces. Low energy helium has also been observed forming hairlike microstructures on single crystal and polycrystalline tungsten. These surface defects and increased porosity accelerate the degradation of materials exposed to the plasma.

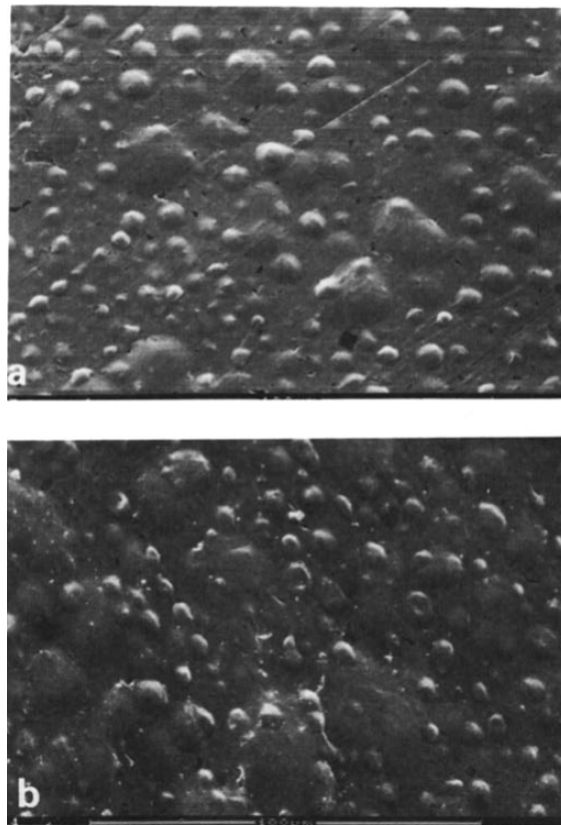


Figure 1.8: SEM images of 316L stainless steel after a) 70 keV He<sup>+</sup> implantation and b) subsequent annealing at 700 K . Reprinted from *Wang 1989* [5].

The results in Figure 1.8 are part of a study carried out at the Beijing University of Science and Technology. In this study 316L stainless steel samples were irradiated with helium ions with energies ranging from 70 keV to 170 keV. These steel samples were irradiated at various temperatures

from 77 to 673 K. Wang et al. found that the critical dose for blistering in 316L increased with He energy, and decreased with sample temperature.

Another low energy helium implantation was carried out by Baldwin and Doerner using the PISCES-B linear-divertor-plasma simulator. In this study polished tungsten discs were exposed to a pure helium plasma at 1120 K and 1320 K for varying lengths of time. The average impact energy of the helium was approximately 60 eV. The samples were exposed for increasing amounts of time and Figure 1.9 shows the evolution of a hair-like nanostructure. During the longest exposure the penetration of this structure into the tungsten was in excess of  $5\ \mu\text{m}$ .

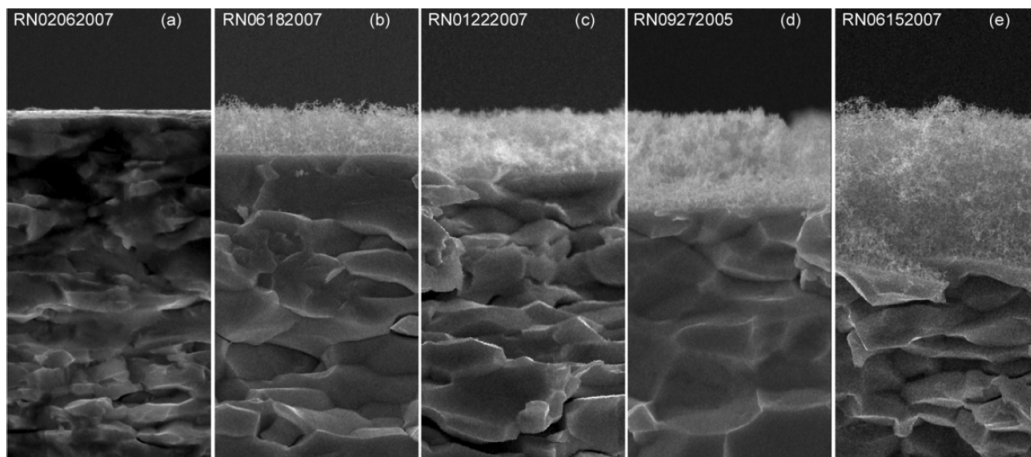


Figure 1.9: Cross-sectional SEM images of W targets exposed to pure He plasma in the PISCES-B for (a) 300 s, (b)  $2.0 \cdot 10^3$  s, (c)  $4.3 \cdot 10^3$  s, (d)  $9.0 \cdot 10^3$  s, (e)  $2.2 \cdot 10^4$  s.  $\Gamma_{\text{He}^+} = (4-6) \cdot 10^{22}\ \text{m}^{-1}\ \text{s}^{-1}$ . Reprinted from *Baldwin and Doerner 2008* [6].

A similar study was carried out at Nagoya University using the NAGDIS-II, a linear divertor plasma simulator. The simulator was used to create helium bubbles in single crystal and polycrystalline tungsten samples. The energy of the plasma began at 1 eV was increased to a range of 100 eV before the conclusion of the experiment [7]. Formation of holes on the tungsten surface were noticeable at energies of 5 eV. In their study it was found that single crystal tungsten was much more resistant to bubble formation than polycrystalline forms.

A dual species irradiation of helium and hydrogen was carried out by Osaka University by Y.

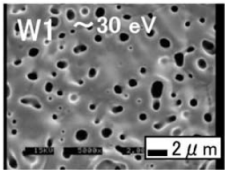
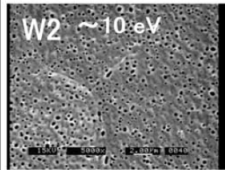
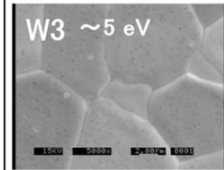
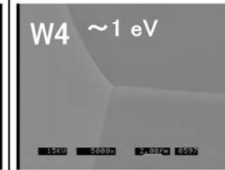
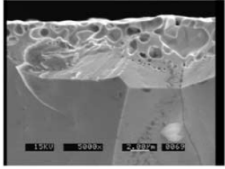
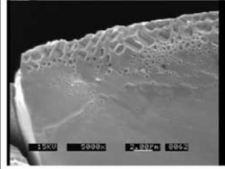
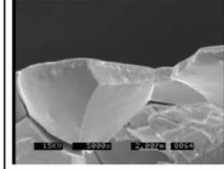
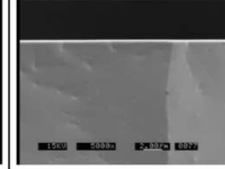
Fluence	$2.6 \times 10^{27} / \text{m}^2$	$0.9 \times 10^{27} / \text{m}^2$	$0.8 \times 10^{27} / \text{m}^2$	$0.8 \times 10^{27} / \text{m}^2$
Ion flux	$3.7 \times 10^{23} / \text{m}^2\text{s}$	$1.2 \times 10^{23} / \text{m}^2\text{s}$	$1.1 \times 10^{23} / \text{m}^2\text{s}$	$1.1 \times 10^{23} / \text{m}^2\text{s}$
Time	7200 s	7200 s	7200 s	7200 s
Temperature	2100 K	2600 K	2200 K	2950 K
Surface				
Cross section				

Figure 1.10: Surface porosity from 1 to 30 eV helium implanted on powder metallurgy tungsten in the NAGDIS-II. Reprinted from *Nishijima 2004* [7].

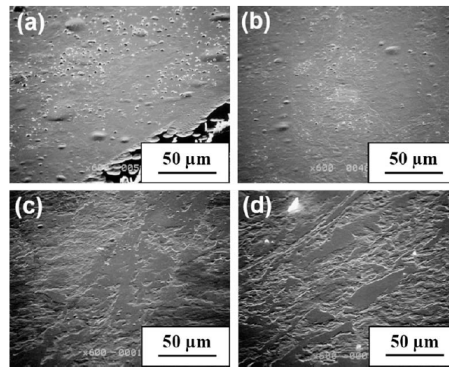


Figure 1.11: Tungsten morphology after H+C+He irradiation at 1 keV . Reprinted from *Ueda 2009* [8].

Ueda et al. In this experiment a H+He+C gas mixture was accelerated at 1 keV towards a tungsten target [8]. It was found that the trace amounts of He in the gas reduced the blistering effect from hydrogen and carbon. The effects of increased helium implantation on the blisters is seen in Figure 1.11.

## 2. EXPERIMENTAL APPROACH

### 2.1 10 kV Accelerator Assembly

The low energy ion source consisted of a rebuilt Colutron Model 100 ion source. This source utilized a tungsten filament and tantalum anode encased in a boron-nitride cup. When energized the arc-discharge between the anode and filament created a cloud of ionizing electrons. When introduced to a gas these free electrons generated positive heavy ions that escape through an opening in the anode.

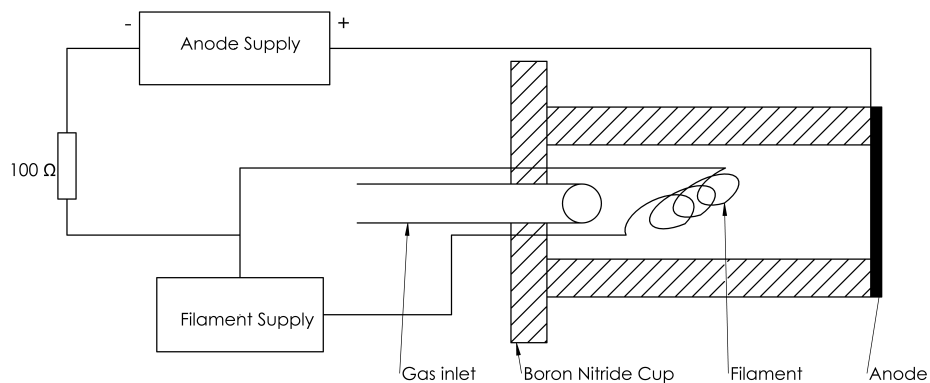


Figure 2.1: Colutron DC ion source schematic.

The  $100 \Omega$  resistor between the filament and anode power supplies served to dampen any instabilities within the plasma once an arc is struck. Figure 2.1 shows the electrical schematic of the ion source apparatus used in this system.

### 2.1.1 Lenses & Optics

This assembly used a series of three lenses to increase or decrease the focus of the beam on its target. This system is referred to as an einzel lens [15]. The first and last lenses in the series were kept at a ground potential with the middle lens was kept at a positive potential that was varied through use of a power source [16]. Figures 2.2 illustrates a decel-accel lens configuration.

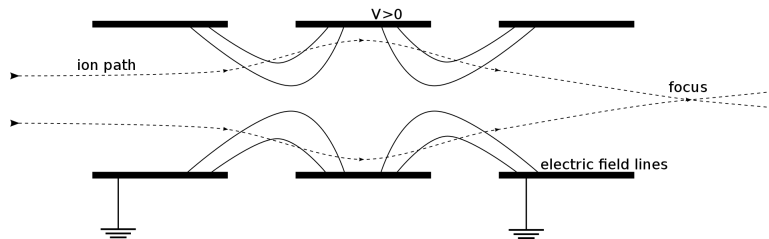


Figure 2.2: Schematic of beam focusing via an einzel lens.

The second grounded lens allowed the focused particles to return to their original energy once through the positively charged lens. By manipulating this focus it was possible to control the incident ion fluence on the final target and provide a more uniform beam spot. The focusing lens assembly was also equipped with two pairs of electrostatic plates that served to steer the ion beam in the vertical and horizontal axes.

### 2.1.2 Magnetic Bending

After the beam was focused by the einzel lens the ions passed through an electromagnetic field orthogonal to the beam direction. The radial acceleration induced by the magnet coupled with the fixed radial path of the beamline allowed the magnetic field to act as both a steering mechanism as well as an isotope selector. The necessary magnetic field required for a specific incident ion to pass through the beamline was calculated by using Equation 2.1 for beam rigidity  $B\rho$  in units of Tesla·m.

$$B\rho = \frac{p}{e} \quad (2.1)$$

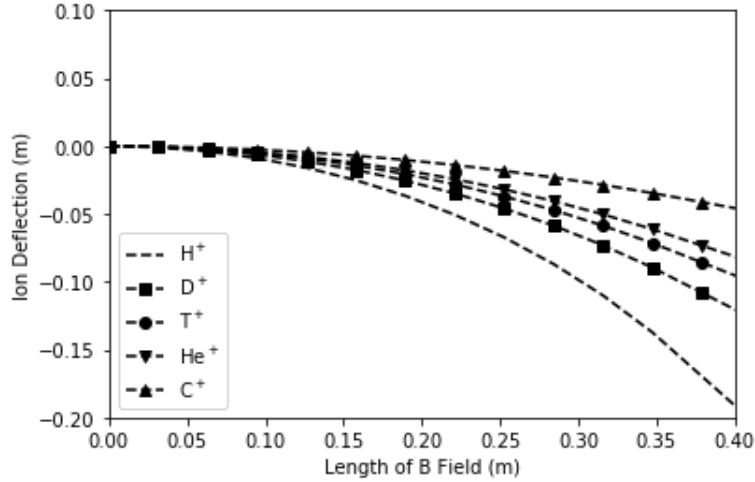


Figure 2.3: Path of various 10 keV ions through a 0.4 m, 283 Gauss field.

Where  $p$  is the momentum of the ion,  $e$  is its electrical charge in Coulombs, and  $\rho$  is the radius of curvature in meters of a particle in magnetic field  $B$  in Teslas [17]. Equation 2.1 can be used to derive Equation 2.2

$$B = \frac{\sqrt{E_{total}^2 - E_{rest}^2}}{300\rho} \quad (2.2)$$

Where  $E_{total}$  and  $E_{rest}$  are given in MeV. The magnet used in this system had two  $15^\circ$  protrusions that each corresponded to a bend radius of 1.016 m and a B-field length of 0.6 m.

Table A.1 was generated by inputting mass data from NIST and the geometry of the bending magnet into Equation 2.2 and assuming an acceleration energy of 0.01 MeV or 0.02 MeV for double charged species [18]. Figure 2.3 shows the path of a selection of ions through a magnetic field.

Solid core electromagnets do have a flaw that must be accounted for when used at low field strengths. Magnetic hysteresis occurs once the core material has reached a magnetic saturation point [19]. This saturation effect can be seen in Figure 2.4. When saturation has been achieved the magnet will carry a residual magnetic field  $m_{r,s}$ .

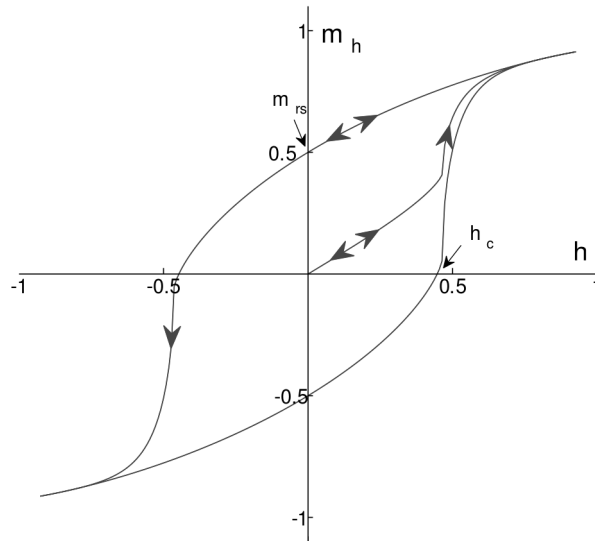


Figure 2.4: Typical hysteresis curve in a solid core electromagnet.

### 2.1.3 Beam Current Measurement

The accelerator was equipped with two charge collection plates that acted as simple Faraday cups following the bending magnet. The collection plate in the  $0^\circ$  beam path was a fixed plate isolated from the accelerator chassis by a ceramic standoff. As the  $0^\circ$  beam path lacked a way to deflect neutral particles carried down the beam line, the  $0^\circ$  collection plate served only as an indicator that the system is producing ions.

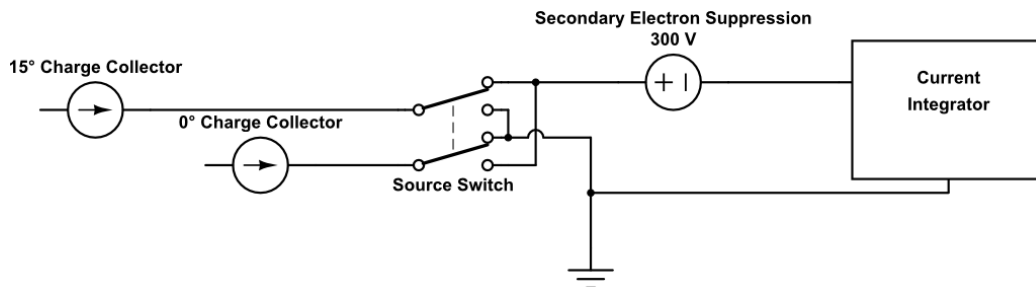


Figure 2.5: Schematic of the collection plate selection switch and current integrator.



The 15° collection plate served to measure the beam current after being separated by the bending magnet. A scintillating quartz crystal with a viewing window followed this plate for visual confirmation of beam size and shape through the experiment. Both the scintillating quartz and 15° collection plate were able to be retracted to allow the ion beam to pass through to the target unhindered. Each collection plate was connected to the DPDT switch shown in Figure 2.5. This circuit allowed the current being passed through the integrator to be switched between 0° and 15° beam paths. The collection plate not being read on the integrator was grounded to prevent any charge buildup while not in use. The 15° cup was preceded by the set of four slits on manual actuators shown Figure 2.6. These slits allowed for precise control of the beam shape on the final target.

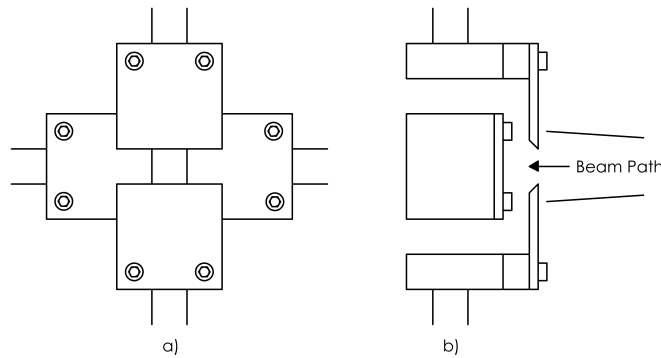


Figure 2.6: Front (a) and side (b) view of the steel slits used to define the beam shape.

#### 2.1.4 Electrical & Safety

To prevent any electrical arcing from the high voltage produced by the accelerator a plexiglass enclosure was built to house the portion of the system containing the ion source, gas inlet valve and electrical connections. The wires leading from the accelerator cabinet to the ion source were fed through flexible PVC tubing which protruded from the base of the plexiglass to provide additional insulation. The source enclosure was secured with lock and key during normal use.

In order to function properly both the anode and filament power supplies were required to float above ground potential. This was achieved by insulating the supplies within plexiglass and connecting the devices to an isolation transformer capable of producing 120 VAC. The output of the Beam Energy supply seen in Figure B.1 is hardwired to the positive anode supply output. This allowed for a single cable to pass from the accelerator cabinet into the ion source enclosure.

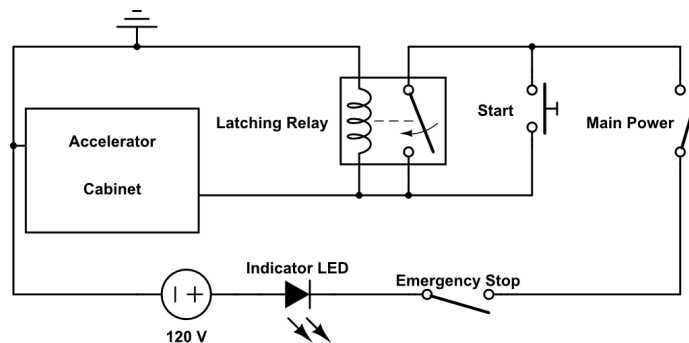


Figure 2.7: Self-latching relay system for an emergency shutdown of the accelerator.

The power supplies and transformer for the acceleration system and bending magnet were stored in a single cabinet equipped with the emergency stop system shown in Figure 2.7. To turn on the device the emergency stop and main power switches were required be closed. If both switches were closed the red Indicator LED stayed lit, indicating the system could be powered on. When the momentary start switch was thrown voltage through the inductor closed the normally-open relay. This relay was on a feedback that ensures as long as the inductor carried power the relay remained closed. Any interruption in power would release the relay and the switches had to be returned to a closed setting before power would resume. This "self-latching" relay configuration prevented any accidental restart of the accelerator after any power failure or emergency shutdown.

### 2.1.5 Vacuum & Cooling Systems

Ultrahigh vacuum pressures are required in linear accelerators for two reasons: Ultrahigh vacuums prevent arc discharge from high voltage equipment and increase the mean free path of ions

within acceleration systems.

The ion source was outfitted with a Pfeiffer-Balzer TBH-330 turbopump and a Varian TP-300 scroll pump. A turbopump system was used over a diffusion pump for two key reasons. Turbopumps drastically reduce the time required to achieve a low enough pressure to begin operating the ion source and do not pose a contamination risk due to oil being drawn into the beamline during use. A thermocouple gauge was used to note the pressure inside the acceleration system for pressures exceeding 50 mTorr. A Gran-Miller ion gauge controller coupled with a Varian ion gauge was used to monitor the internal pressure once it fell below 50 mTorr.

A bracket was connected to the TBH-330 source onto which two 140 mm 120 VAC fans were mounted to provide cooling to the turbopump during use. The ion source came equipped with a heat sink flange designed to prevent overheating during long periods of use. A Copeland FBAH-A025 compressor was connected to the heat sink to maintain an ion source temperature below 100 °F. This model compressor was originally designed for use with R-12 refrigerant. As R-12 has been discontinued as a refrigerant and was difficult to procure this the compressor was retrofitted to use the modern R-134a coolant. The compressor was wired in parallel with the main power line into the accelerator cabinet. This removed the ability to power on the ion source without engaging the cooling system.

### **2.1.6 System Alignment**

To ensure a maximized beam transmission the acceleration system was aligned both vertically and horizontally. Each component of the system rested on four threaded feet allowing for vertical adjustment. Using a bubble level and square center marks were made on the top and left side of each flange down the beam line. A surveyor's laser was then used to note a level horizontal plane. The center of the ion source gas inlet was used as a reference and each component was raised or lowered until their center marks fell in line with the laser. This process was repeated in the vertical plane to ensure the resulting ion beam would not crash into a surface prior to reaching the target. Figures 2.8 and 2.9 illustrate this process.



Figure 2.8: Vertical laser alignment.



Figure 2.9: Horizontal laser alignment.

## **2.2 1.7 MV Plasmatron/SNICS**

### **2.2.1 Duoplasmatron Source**

The Duoplasmatron source shown in Figure 2.10 works on a similar principle as the 10 kV ion source. Gas is fed through an inlet and ionized by free electrons before being accelerated through an aperture and einzel lens focusing element. The difference in using the Duoplasmatron is that there is no arc taking place within the ion chamber. The ion chamber is walled with ferritic iron and surrounded by an electromagnet. When a current is passed through the platinum coated filament thermal electrons are released which ionize the gas coming through the inlet. This creates a diffused plasma inside the ion chamber close to the gas inlet.

The tapered magnetic design of the source moves the free electrons and positive ions towards the extraction voltage. This magnetic field forces the ions into dense plasma near enough to the extraction cup to allow positive ions to be accelerated towards the target. This two plasma design is where the Duoplasmatron gets its name.

The ions that are accelerated out pass through a charge exchanger after being focused by an einzel lens. This exchanger vaporizes liquid sodium (Na) in the path of the beam. Sodium has a weak electronegativity and will readily give up electrons to the passing positively charged ions. When a given ion accrues an excess electron it will become negatively charged and continue traveling down the acceleration column and into the pre-acceleration column.

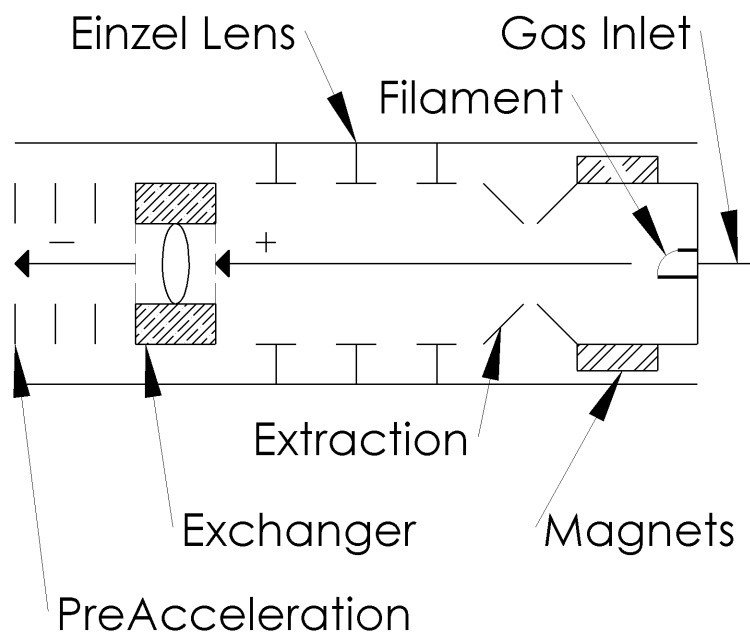


Figure 2.10: Duoplasmatron source diagram.

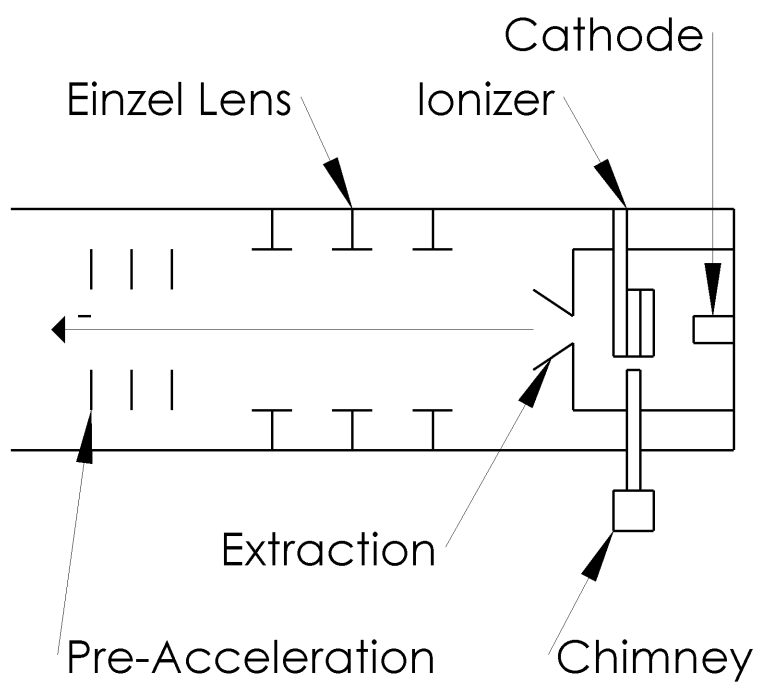


Figure 2.11: SNICS source diagram.

### **2.2.2 SNICS Source**

The SNICS source in Figure 2.11 utilizes a cesium chimney and a solid cathode to generate ions. The cesium begins in a liquid stage loaded into a heater and loaded at the base of the chimney. As the cesium is heated it vaporizes and travels up the chimney and into the ionizing chamber. A portion of the cesium will coat the cathode loaded into the material while the rest become positively charged by colliding with thermal electrons emitted by the ionizer. This charged cesium is accelerated by a positive voltage towards the cathode and knock the target atoms free. These target atoms travel through the cesium layer deposited on the cathode surface and become negatively charged by pulling electrons from the cesium as they pass. These negative ions are then accelerated by the extraction cup and into the pre-acceleration column. As the ions are negative by default the SNICS does not need a charge exchange prior to the main acceleration column.

### **2.2.3 Low Energy Filter Magnet**

After each pre-acceleration column the two sources are joined to one beamline in the low energy filter magnet. This magnet operates on the same principle as the filter magnet in the 10 kV acceleration system. Ion paths passing through the magnet are bent by changing the current through the magnet until the desired ion species is passing through the main acceleration column. This magnet is essential to the two source design without the ability to steer the ions only a single source could be mounted to the acceleration column.



## **2.2.4 Acceleration Column**

The main acceleration column gets the Tandem name from the fact that it is actually two acceleration columns working together. The first column in Figure 2.12 is used to draw the negatively charged ions into a canal flooded with a nitrogen gas. This stripper chamber serves to remove any excess electrons from the ion beam and allow only positively charged ions to leave the chamber towards the target. The second column is used to accelerate the ions to their final energy before leaving the chamber.

The acceleration voltage in this design is achieved by using a Cockcroft-Walton Ladder. This assembly of pentodes and capacitors allows an AC current to be rectified into a DC current that is stepped up to 1.7 MV. This terminal voltage is placed on the stripper chamber while the two columns at either end are kept at ground potential.

## **2.2.5 High Energy System**

After the main acceleration chamber the ions are passed through a quadrupole focusing magnet. This magnetic element serves to refocus the ion beam on its path through the nitrogen chamber and subsequent acceleration through the second column. After being re-focused the beam is bent using a final high energy magnet to the desired target chamber. Each target chamber as well as the acceleration system are kept at an ultrahigh vacuum through a mixture of turbo-molecular and ion pumps.

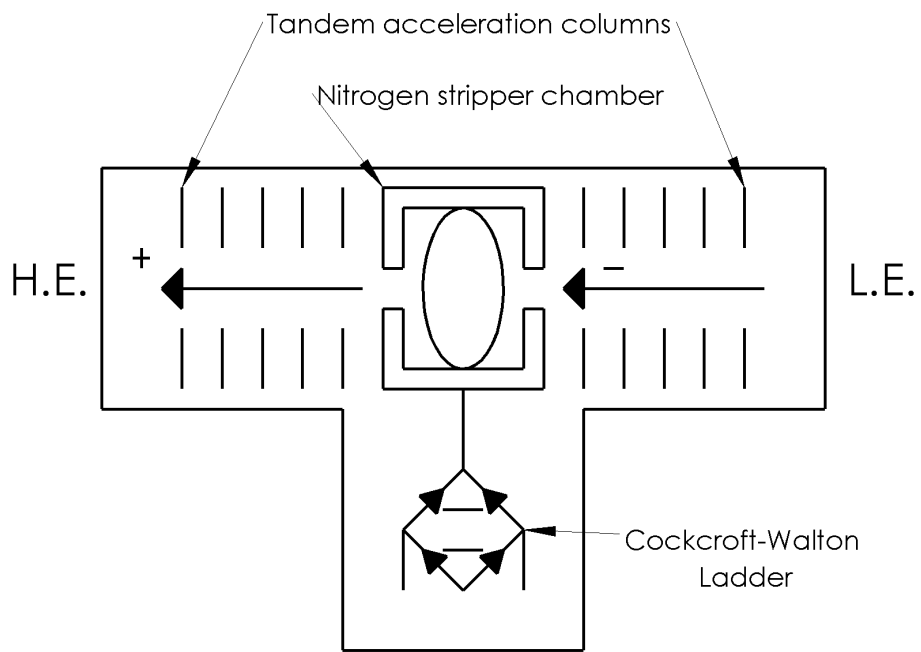


Figure 2.12: Tandem acceleration column diagram.

### 2.3 Target Chambers

The target chamber pictured in Figures 2.13 was connected to the acceleration system by a pneumatic gate valve. The target sample stage consists of a stainless steel plate mounted to a single axis manual goniometer with a brass fitting and set screw. The stage is not isolated electronically from the chamber to prevent charge buildup on the target stage during implantations.

When the gate valve was closed this chamber could be vented and the stage removed. This allowed for a change of targets without the need to shut down the 10 kV acceleration system between implantations. Once the stage had been remounted and moved into the desired position on the goniometer indicator the chamber could be pumped back down via a roughing pump before opening the gate valve to the acceleration system.

The multibeam chamber shown in Figure 2.14 was already attached to both the 1.7 MV Plasmatron/SNICS source and the 400 kV ion source. This chamber had a top port that multiple stages could be loaded into. For the experiments carried out for this thesis an Inconel stage equipped with a thermocouple heater was used. This hot stage had a dual axis goniometer allowing the target to be rotated to adjust the striking angles of the incident beams and to be adjusted up or down vertically for alignment. In addition to having its own turbopump system the multibeam chamber was also equipped with a liquid nitrogen cold trap. The combination of cold trap and turbopump allowed this chamber to reach pressures in the  $10^{-8}$  Torr range.

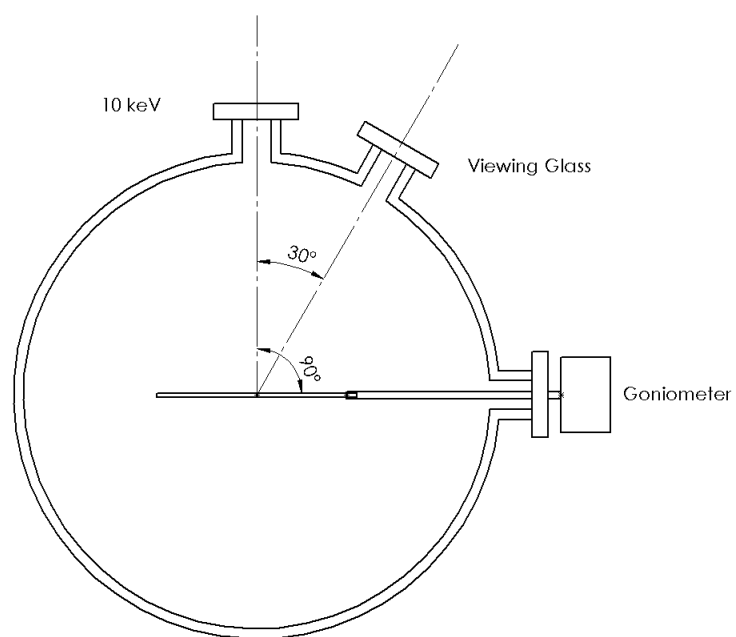


Figure 2.13: Target chamber geometry, top down view.

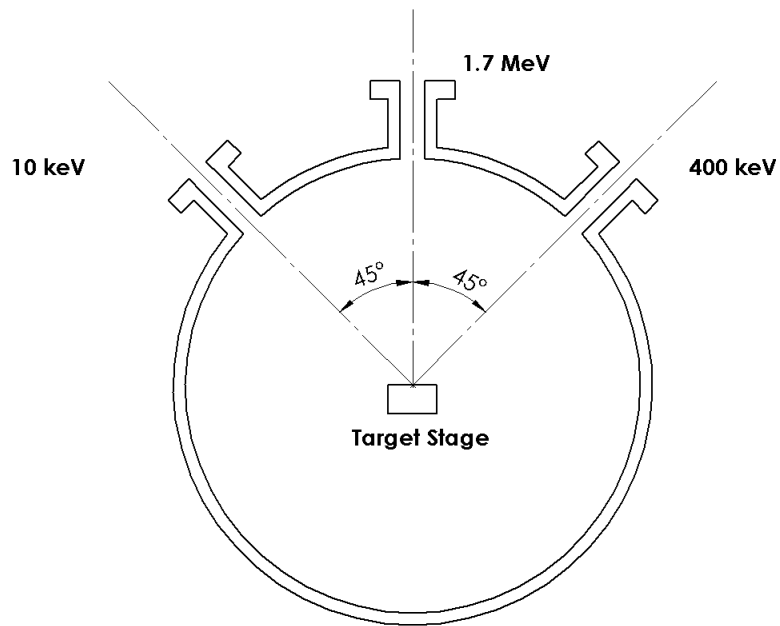


Figure 2.14: Multibeam chamber geometry, top down view.

## 2.4 Calibration Experiments

A series of beam current measurements, magnet current adjustments, and an implantation were performed to assess the capabilities of the 10 kV accelerator prior to the dual beam experiment. Prior to powering on the ion source the system was pumped down to an ultra-high vacuum in two stages. The first stage was done with the rough pump connected in line with the turbopump. The second stage began once the vacuum in the system reached 50 mTorr. The gate valve separating the target chamber was left open to ensure the initial vacuum in the chamber matched the vacuum in the acceleration system.

Once the system reached a pressure below  $10^{-6}$  Torr the emergency stop switch was disengaged and power was supplied to the accelerator cabinet. After confirming the coolant compressor powered on with the cabinet the filament and anode power supplies were switched on. The anode was first left at 0 V while the filament voltage was increased by approximately 1 V every 120 seconds. This method allowed the filament time to heat up slowly to prevent damage to both the filament and ion source. This also prevented rapid outgassing from overloading the turbopump. Once the filament reached the target current (between 10-15 amps) the anode voltage was raised to an initial value of 150 V.

Once the filament and anode voltage were at operational values the beam energy voltage was raised to 10 kV and the needle valve leading to the helium supply was slowly opened until an arc current was struck between the filament and anode. This current was displayed on the anode supply and had an operational range of 300 mA to 450 mA. At this point the current integrator was powered on and set to the  $0^\circ$  collection plate to measure an initial beam and find an optimal focus voltage for the einzel lens system.

### 2.4.1 Ion Identification

With a beam established the first procedure was to identify the species being produced inside the ion source. This was accomplished by switching the current integrator to the  $15^\circ$  collection plate and slowly raising the current in the bending magnet until a beam current registered on

the integrator. The magnet current was recorded and divided by the magnet current presumed to correspond the  $\text{He}^+$  peak.

Figure 2.15 plots the magnetic field in Gauss required for the first eight elements of the periodic table as well as deuterium and tritium to pass through the  $15^\circ$  beam path and strike the charge collection plate.

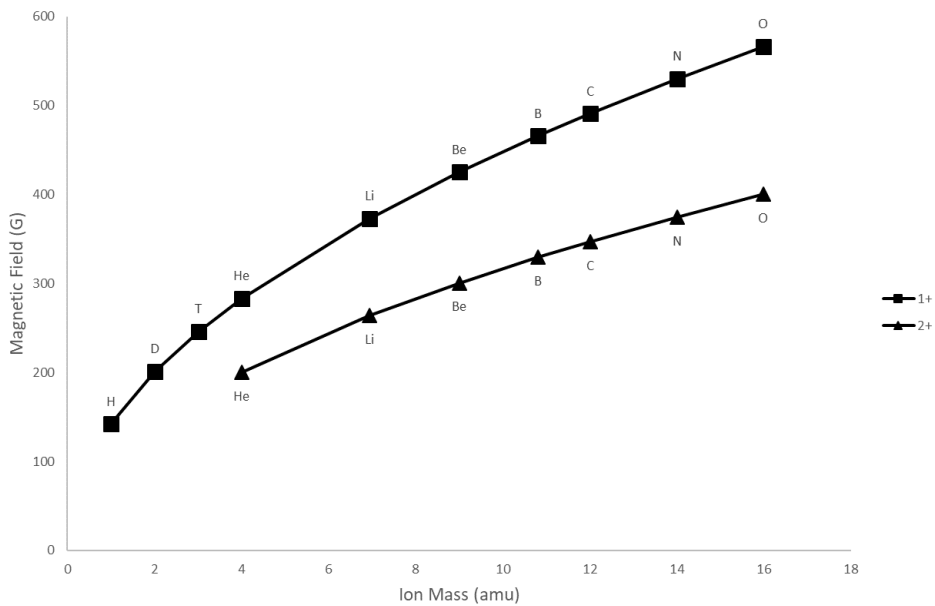


Figure 2.15: Magnetic field for a given ion to bend at a 1.016 m radius at 10 keV.

Using Ampere's Law:

$$B = \frac{NI}{L} \quad (2.3)$$

Where  $N$  is the number of turns in the coil of an electromagnet,  $I$  is the current traveling through the coil, and  $L$  is the length of the magnet core. Given that  $N$  and  $L$  are constant it can be said that:

$$\frac{B_i}{B_{\text{He}^+}} = \frac{I_i}{I_{\text{He}^+}} \quad (2.4)$$

Thus using Equation 2.4 the current ratios were compared to the  $B:B_{\text{He}^+}$  ratios found in Table A.1

to identify which ion that beam current consisted of.

The scanning process was performed four separate times. The first two scans were performed with the vertical slits fully open and the horizontal slits opened to 10 mm. The gas supply for the first two scans was a bottle of welding grade helium. To reduce potential contamination the gas supply bottle was exchanged for a high purity helium bottle and the system was left at a vacuum near  $4 \cdot 10^{-7}$  Torr for a period of 24 hours to allow further outgassing to occur prior to extended testing. The third and fourth scans were performed with the slits positioned to allow a 6x6 mm beam spot to strike the collection plate.

#### **2.4.2 Beam Uniformity**

A qualitative analysis of the flux uniformity was conducted by performing a "burn-in" where paper was used to monitor the beam profile for focused and neutral beam effects. Plain white 20 wt. paper was fixed to both sides of the stage in the target chamber and the slits were left at a 6x6mm opening. The stage was rotated until the beam path was orthogonal to the target paper. A beam current of 300 nA was reached and the scintillating quarts and collection plate were withdrawn from the beam path for 240 seconds. Once one side of the stage had been burned in the collection plate was lowered and the stage was rotated 180° with the goniometer and the burn in process was repeated for another 240 seconds. The paper targets were removed from the target chamber and the resulting beam spot was measured using a precision ruler and examined for dark spots that would indicate over focusing or neutral beam being generated after the bending magnet.

After attaching the acceleration system to the multibeam chamber two pairs of steering magnets were set up prior to the slits to raster the beam over the target area. Each pair of magnets was controlled by a function generator that swept the beam left to right and up and down the target area in a saw tooth pattern. This rastering technique removed the uneven portions of the beam spot and provide a more uniform distribution of ions across the sample surface.



## 2.5 Mass Resolution

The resolving power of a system is its ability to separate two distinct masses within a certain distance. In this accelerator system the resolution was determined by examining the angle between the trajectory of two given ion species and the distance these ions will travel apart from each other before passing through the slits.

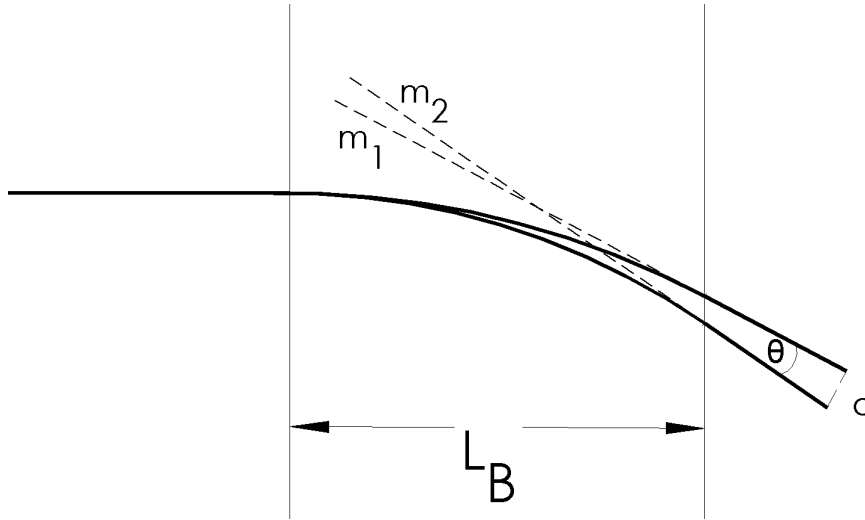


Figure 2.16: Beam paths with tangent trajectories.

The distance  $d$  in Figure 2.16 was set to 5 mm as this was the maximum slit opening used in each experiment. The ratio of two given ions was found by using the Larmor radius and kinetic energy of each ion found in Equations 2.5 and 2.6.

$$r = \frac{mv}{qB} \text{ and } v = \sqrt{\frac{2E_{ac}q}{m}} \quad (2.5)$$

$$r^2 = \frac{2E_{ac}qm}{q^2B^2} \quad (2.6)$$

Relativistic equations were disregarded for this calculation as the maximum velocity achievable by a given ion in this accelerator is well below the speed of light. The Larmor radius is squared in

Equation 2.7. This value became useful in subsequent calculations. It was noted that the kinetic energy of a given ion will be the product of the acceleration voltage  $E_{ac}$  and the ion's elemental charge  $q$ . Each ion experienced the same  $E_{ac}$  and passes through the same magnetic field  $B$ . When their ratios were calculated these values disappeared and left only masses  $m_i$  and charges  $q_i$  in Equation 2.7

$$R_{m,q} = \frac{r_2^2}{r_1^2} = \frac{m_2 q_1}{m_1 q_2} \quad (2.7)$$

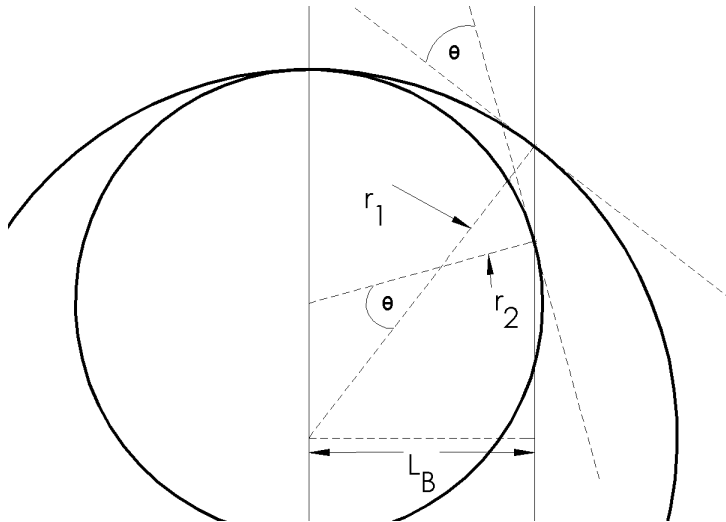


Figure 2.17: Geometry of beam path.

It was useful to view the separate beam paths as full circles whose center points were co-linear as in Figure 2.17. The beam paths would leave the magnetic field on a fixed trajectory that was tangent to this circle at that point. The slope  $m_i$  of a given beam path was calculated in Equations 2.8 from the length of the magnet  $L_B$  and the larmour radius  $r_i$ .

$$m_i = \frac{\sqrt{r_i^2 - L_B^2}}{L_B} \quad (2.8)$$

The angle between two intersecting lines was calculated from their slopes in equation 2.9.

$$\theta = \arctan\left(\pm \frac{m_1 - m_2}{1 + m_1 m_2}\right) \quad (2.9)$$

Substituting Equation 2.9 for  $m_1$  and  $m_2$  yielded Equation 2.10.

$$\theta = \arctan\left(\pm \frac{\frac{\sqrt{r_1^2 - L_B^2}}{L_B} - \frac{\sqrt{r_2^2 - L_B^2}}{L_B}}{1 + \frac{\sqrt{r_1^2 - L_B^2}}{L_B} \frac{\sqrt{r_2^2 - L_B^2}}{L_B}}\right) \quad (2.10)$$

Which could be simplified into Equation 2.11.

$$\theta = \arctan\left(\pm \frac{\sqrt{r_1^2 - L_B^2} - \sqrt{r_2^2 - L_B^2}}{\sqrt{r_1^2 - L_B^2} \sqrt{r_2^2 - L_B^2} + L_B^2}\right) \quad (2.11)$$

By assuming  $r_1$  was a fixed value for the species that was deflected perfectly down the beamline  $r_2$  could be expressed in terms of  $r_1$  by using the relationship in Equation 2.8

$$\theta = \arctan\left(\pm \frac{\sqrt{r_1^2 - L_B^2} - \sqrt{R_{m,q} r_1^2 - L_B^2}}{\sqrt{r_1^2 - L_B^2} \sqrt{R_{m,q} r_1^2 - L_B^2} + L_B^2}\right) \quad (2.12)$$

When Equation 2.12 was plotted as  $\theta(R_{m,q})$  it yielded two distinct lines in Figure 2.18. The acute angle represented the angle formed between two separate ion paths as they left the magnet. This angle combined with the distance from the magnet to the slits yielded the maximum distance  $d$  two given ions will have between them as they pass through the slits. In the geometry for the 10 kV accelerator it was determined that ions with a  $R_{m,q}$  between approximately 0.95 and 1.05 would not be able to be resolved. This meant that ions with near identical mass to charge ratios could not be separated using this system.

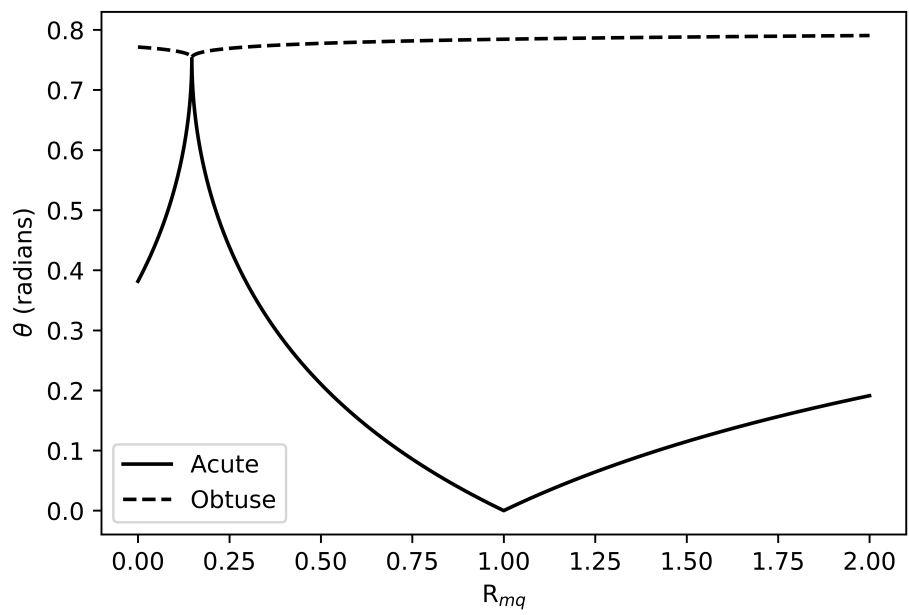


Figure 2.18:  $\theta$  as a function of  $R_{m,q}$ .

## **2.6 Helium Implantation in 316L Stainless Steel**

### **2.6.1 Sample Preparation**

Stainless steels are ubiquitous in a number of scientific applications. 316L stainless steel was chosen as a target material due to the wealth of data from previous radiation damage experiment. In past proposals for the ITER project 316L was also considered for a blanket material for the first wall. 316L is a Cr-Ni-Mo alloy with a face-centered cubic structure. The addition of molybdenum into the alloy provides it with improved corrosion resistance. Of the three phases of stainless steels, austenitic is the only phase that is not ferromagnetic.

A batch of 316L samples were prepared first by bulk cutting the samples into roughly 5x5 mm squares with a silicon carbide cutting wheel. Each square was then mechanically polished with fine grit paper beginning at P400 grit and ending with a P4000 grit pad. A cloth finishing pad was then mounted onto the polishing wheel and loaded with a 0.25  $\mu\text{m}$  diamond solution. The final polish was done with a 0.04  $\mu\text{m}$  colloidal silica solution. After polishing the samples were bathed in acetone and cleaned via sonic vibration before being wiped with methanol and finally placed in a desiccator to remove any residual moisture.

### **2.6.2 Stage Preparation**

A paper sample was mounted to the hot stage in the multibeam chamber. A beam current of 550 nA was focused on the charge collection plate and rastered by steering the beamline in both the horizontal and vertical axes until the current on the integrator read 300 nA.

A cut of plain white paper was mounted onto the Inconel stage as seen in Figure 2.19 and was subjected to the beam for 15 minutes to produce a burn spot dark enough to distinguish. This spot was cut out with a razor blade and the steel sample was fixed to the stage using a colloidal silver paste as adhesive.

Figure 2.20 shows the sample mounted within the marks left on the stage from cutting the burn spot out to the target paper. The stage and sample were then loaded into the multibeam chamber and the stage was rotated until the sample surface was normal to the 10 kV beam path. The pressure

in the chamber was lowered first by a rough pump to 50 mTorr and then down to 0.5  $\mu$ Torr with the turbomolecular pump.

Once the pressure of the chamber dropped to 0.5  $\mu$ Torr liquid nitrogen was added to the cold trap to bring the chamber pressure down further to approximately  $8 \cdot 10^{-8}$  Torr. Once a suitable vacuum was reached the temperature of the stage was raised to 475  $^{\circ}$ C by slowly increasing the power in the heater over the course of 3 hrs while monitoring the temperature via a thermocouple mounted to the back side of the stage. Once the sample reached the desired temperature the charge collection plate was withdrawn from the beamline path and the sample was irradiated for 5 hrs.

Due to the temperature of the stage it was not possible to measure the beam current on the target directly with an integrator. Instead every 30 min the collection plate was lowered for 10 s and the average beam current was found to ensure the beam current had not shifted significantly. Once the sample had reached its 5 hr mark the beam was turned off and the gate valve separating the target chamber and the beamline was closed.

The sample was allowed to cool for approximately 15 hours in a vacuum not exceeding  $5.0 \cdot 10^{-7}$  Torr until the temperature was approximately 35  $^{\circ}$ C. Allowing the sample to slowly cool prevented thermal shock to both the stage and sample.



Figure 2.19: Burned paper marking beam spot

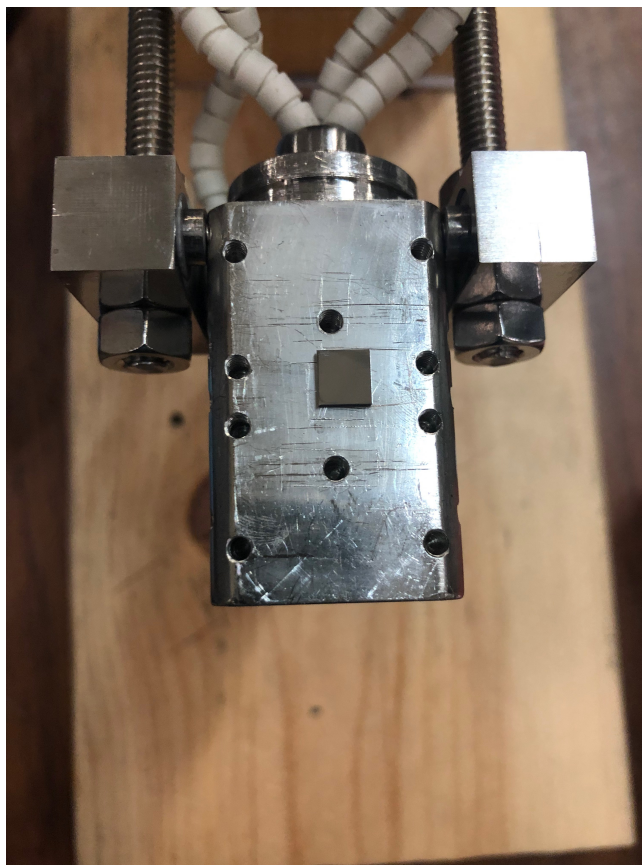


Figure 2.20: 316L sample mounted to Inconel hot stage.



## 2.7 Dual Implantation in 316L Stainless Steel

For the dual ion beam experiments a half & half approach was used to subject different segments of the same target to two separate incident ion beam compositions. This approach made it possible to maintain a uniform helium deposition across an entire sample while one segment was also bombarded with iron. To begin this process another cut of plain paper was fixed to the Inconel stage. The stage was then lowered into the vacuum chamber and positioned such that the stage surface was normal to the 1.7 MV beamline and the 10 kV beamline was incident at a 45 ° angle. The target chamber pressure was reduced and a 1  $\mu\text{A}$  beam of 10 keV  $\text{He}^+$  ions was used to burn a spot into the target paper.

A second 100 nA beam of 3.4 MeV  $\text{Fe}^+$  ions from the SNICS source was then used to make a second burn spot on the target. Adjustments to the slits and steering magnets were made on both accelerators until the beam spots overlapped as shown in Figure 2.21. The measurements of these burn spots used to calculate fluxes are shown in Figure 2.22.

Once a significant portion of the beams were overlapping the area of interest was cut out of the target paper and the sample was fixed to the Inconel stage with silver paste. Each of the samples were placed so that the incident ions struck the sample surface in the pattern in Figure 2.23.

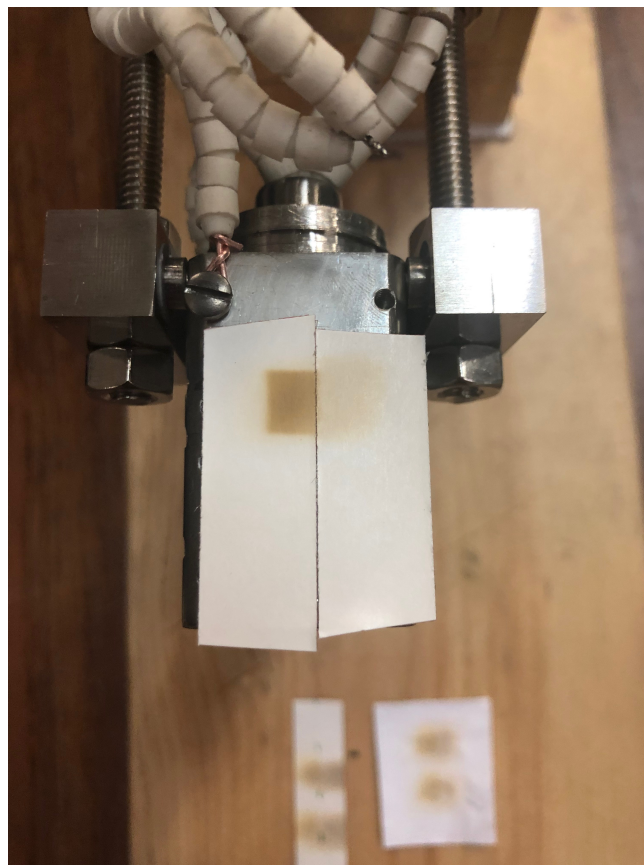


Figure 2.21: Overlapped Fe and He beam spots.

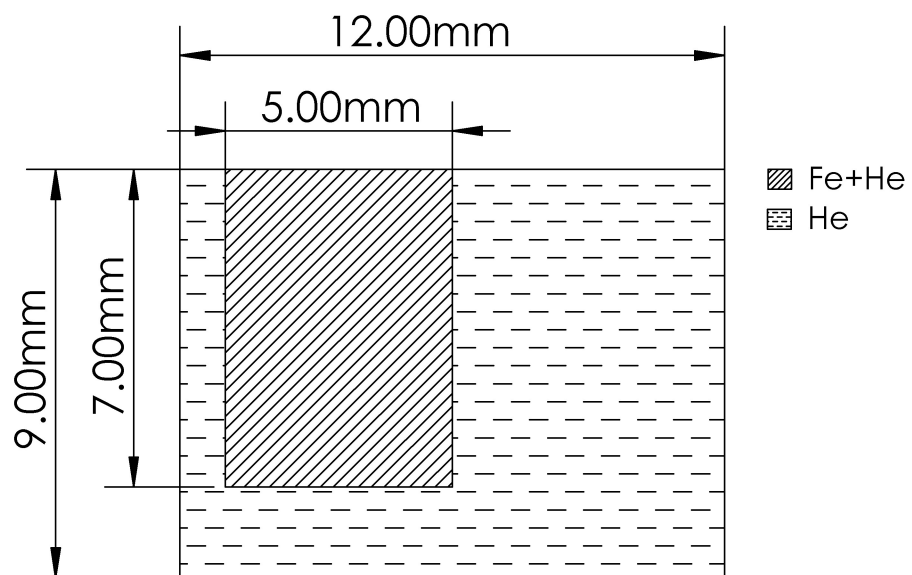


Figure 2.22: Overlapping beam spot measurements.

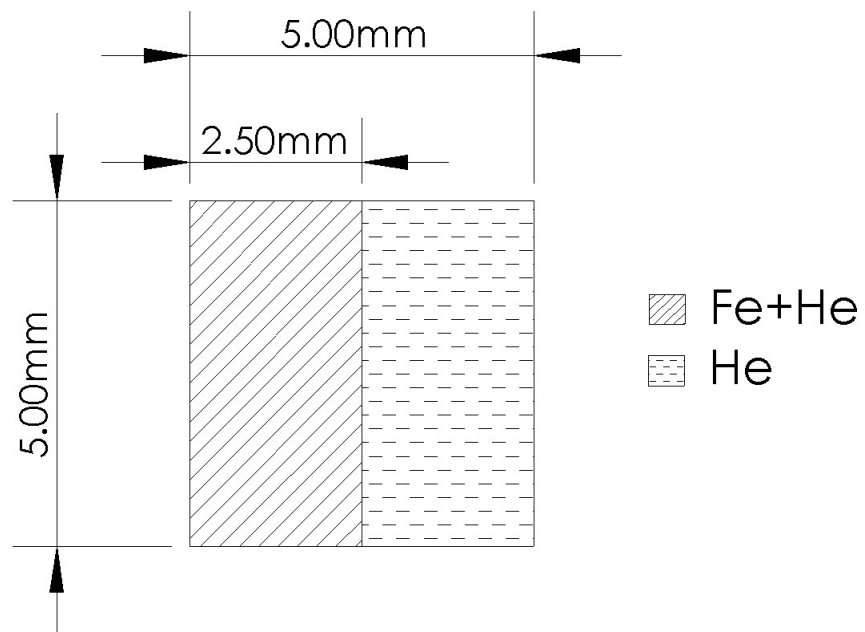


Figure 2.23: Pattern of irradiation across dual beam samples.

Table 2.1: Fluences and temperatures for dual beam implantations.

Target $\Phi$ (ions·cm <sup>-2</sup> )	$\Phi_{He,final}$ (ions·cm <sup>-2</sup> )	$\Phi_{Fe,final}$ (ions·cm <sup>-2</sup> )	T (°C)
$5.0 \cdot 10^{15}$	$4.824 \pm 0.48 \cdot 10^{15}$	$5.096 \pm 0.51 \cdot 10^{15}$	$475 \pm 3$
$3.0 \cdot 10^{16}$	$2.98 \pm 0.29 \cdot 10^{16}$	$2.89 \pm 0.28 \cdot 10^{16}$	$475 \pm 3$

After the silver paste was cured via heat gun the stage was lowered back into the multibeam target chamber with the sample face normal to the 1.7 MV beam line. The pressure in the target chamber was lowered to  $8 \cdot 10^{-8}$  Torr before the stage temperature was raised to 475 °C. Once the sample surface reached 475 °C the Faraday cup in the 1.7 MV beamline and the charge collection plate in the 10 kV beamline were removed and ions began bombarding the sample. This process was carried out for two separate fluences.

The target fluences for the two experiments were  $5.0 \cdot 10^{15}$  ions·cm<sup>-2</sup> and  $3.0 \cdot 10^{16}$  ions·cm<sup>-2</sup> for each species of ion. The currents of each beam and surface temperature of the samples were recorded at 30 min intervals and settings were adjusted to ensure the final fluences would be equivalent at the end of each implantation. The average temperature and final fluences are shown in Table 2.1. Once each implantation finished the accelerator systems were shut down and the sample was left in a vacuum no more than  $6 \cdot 10^{-7}$  Torr to cool overnight. After the samples reached a temperature below 35 °C they were removed from the target stage and placed in a dessicator to reduce exposure to moisture until microscopy could be performed.

## 2.8 FIB Preparation and TEM Analysis

### 2.8.1 FIB Etching

A cross-section of each sample half was used to determine the radius and depth of helium bubbles within the target. These cross-sections were generated by carving out a thin lamella of the sample using a focused ion beam (FIB). FIB etching uses a heavy ion beam to sputter away atoms from a sample to cut out the desired shape. In the LYRA3 system used for this experiment the etching beam was comprised of 30 keV Ga ions. A secondary electron beam was used in tandem with the gallium to perform scanning electron microscopy (SEM) during the etching process.

The FIB process started by examining the surface of the sample under the SEM until a grain large enough to cut an approximately 10  $\mu\text{m}$  wide lamella was found. Before beginning the etching process the region of interest was coated with a protective platinum layer shown in Figure 2.24. This layer was created by spraying a focused 150 pA beam of platinum ions on the surface. The platinum film prevented the gallium from etching away the region of interest as the lamella was carved out.

Once the platinum layer was thick enough the gallium beam was used to cut deep trenches on either of the region of interest. a high beam current was used to carve out these trenches in the staircase pattern seen in Figure 2.25. Afterwards the beam current was lowered to smooth the sample out and thin the sample down to the point that a single layer of bubbles would be visible under the TEM. Once the lamella had reached the desired thickness a series of three cuts often called a "J-cut" were made to remove the lamella from the bulk sample as seen in Figure 2.26.

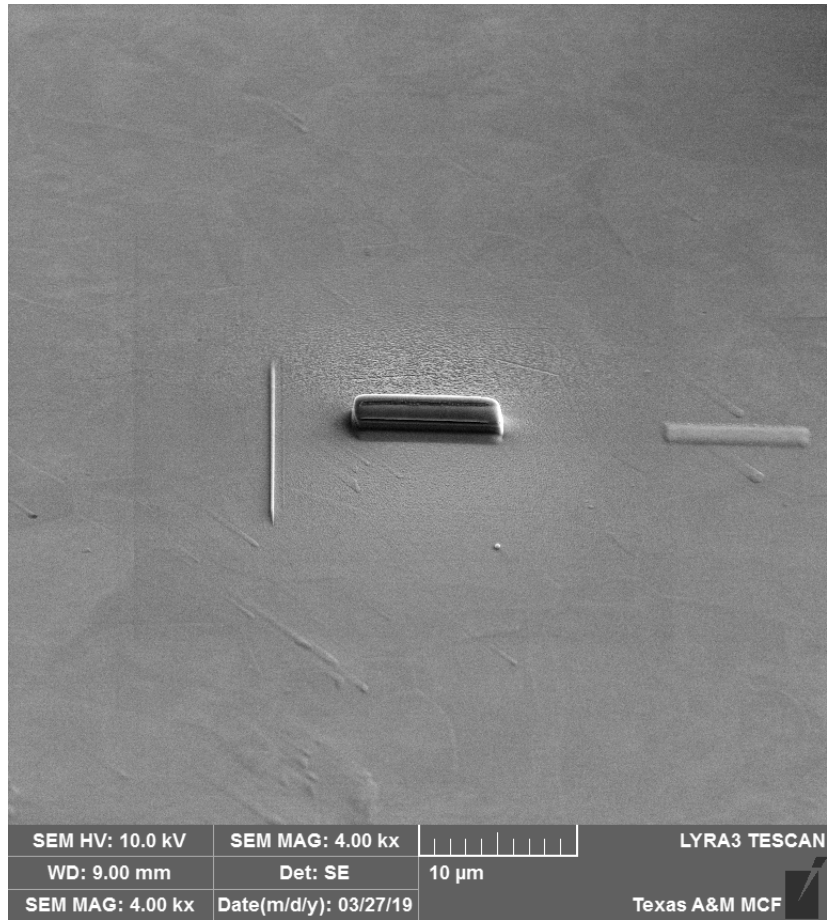


Figure 2.24: Platinum buildup on sample surface.

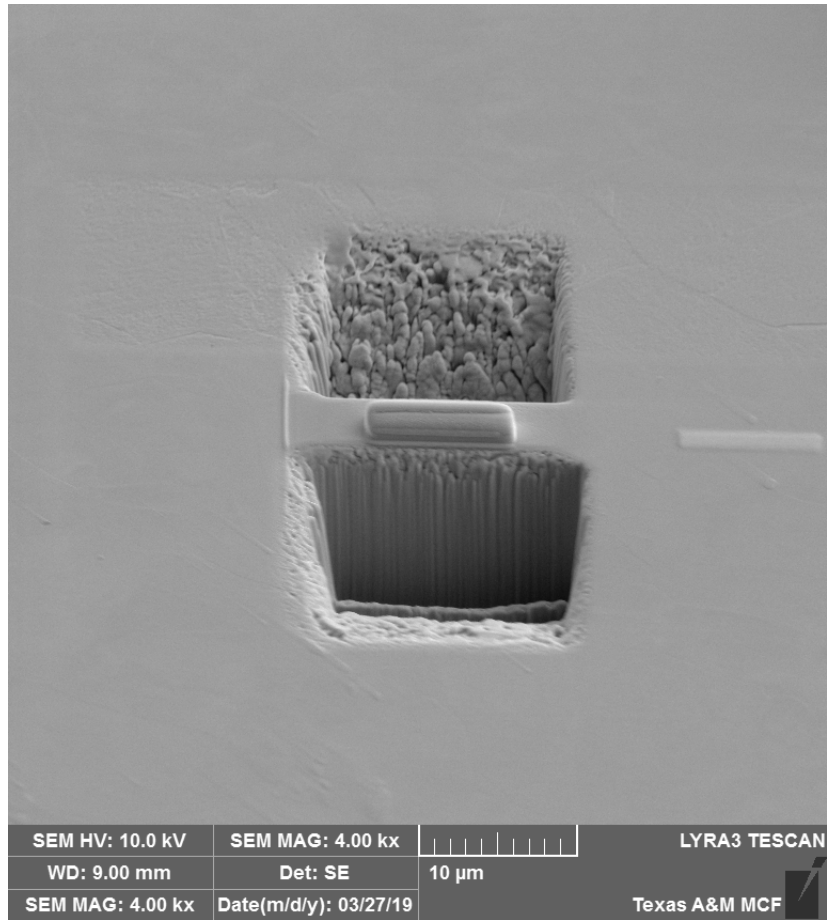


Figure 2.25: Troughs cut to form thin lamella for TEM imaging.



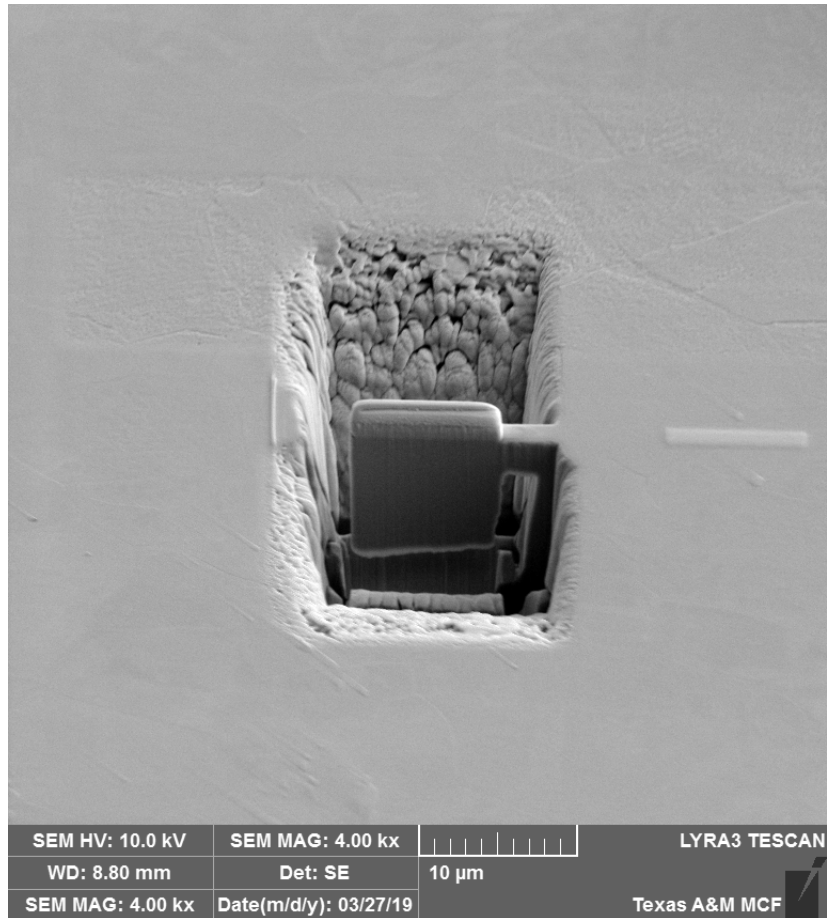


Figure 2.26: J-cut made into lamella for lift out procedure.

A needle probe was brought to the sample and welded to the free edge of the lamella with additional platinum. With the lamella securely fixed to the probe the remaining edge material was etched away and the bulk sample was moved away from the probe. A TEM grid was brought close to the probe and the lamella was fixed to the grid with platinum before the probe was cut free. Figures 2.27 and 2.28 show the the lamella freed from the bulk sample and fixed to the TEM grid. This process was repeated for each of the single and dual beam samples.

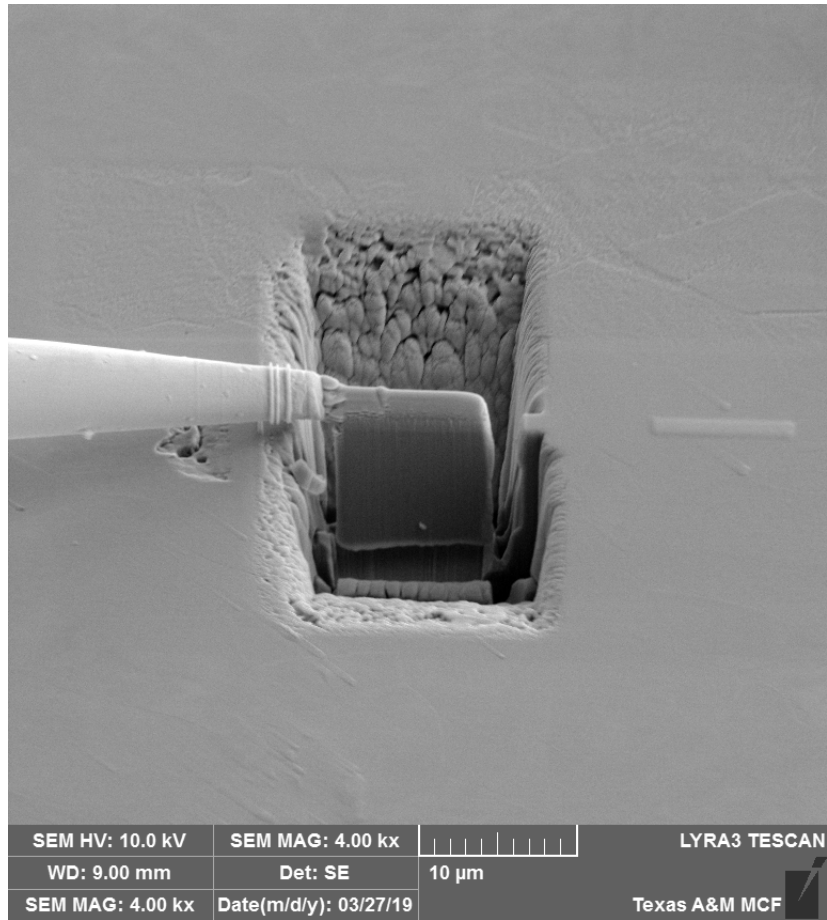


Figure 2.27: Lamella welded to probe with platinum and cut from bulk sample.

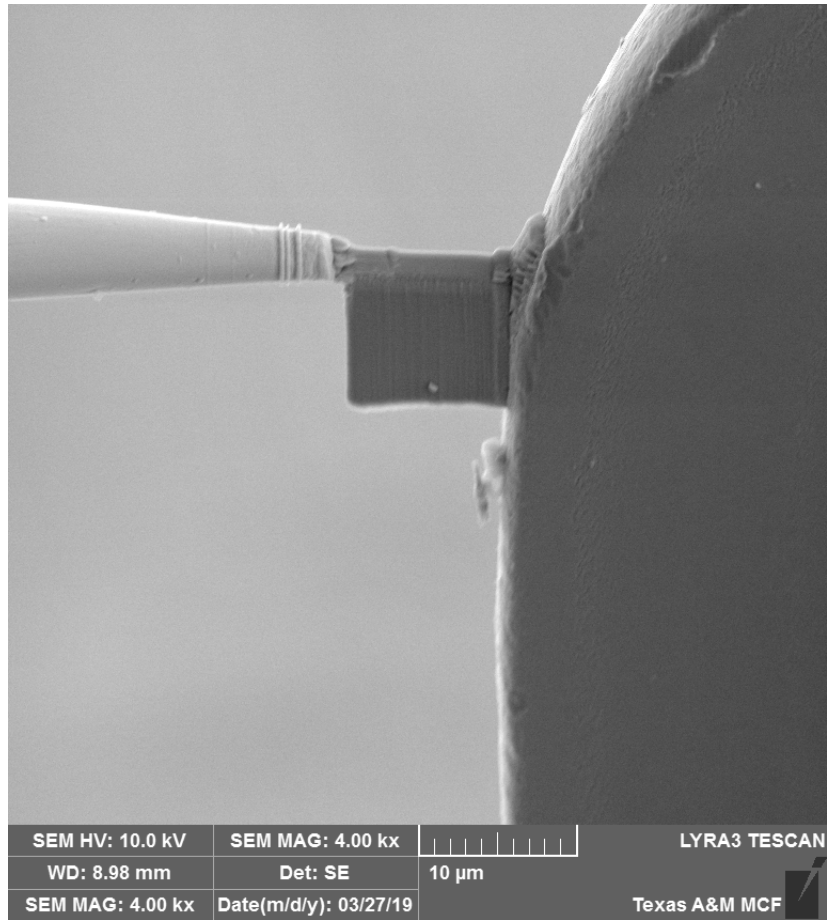


Figure 2.28: Lamella welded to TEM grid ready for imaging.

## 2.8.2 TEM Imaging

Each lamella was viewed under a transmission electron microscope (TEM) to determine the effects of the ion implantation. TEM uses a beam of electrons passed through the object in question and a detector to observe the interactions of the electrons in the material and form an image. TEM is useful when looking at structures that are too small for visible light to resolve.

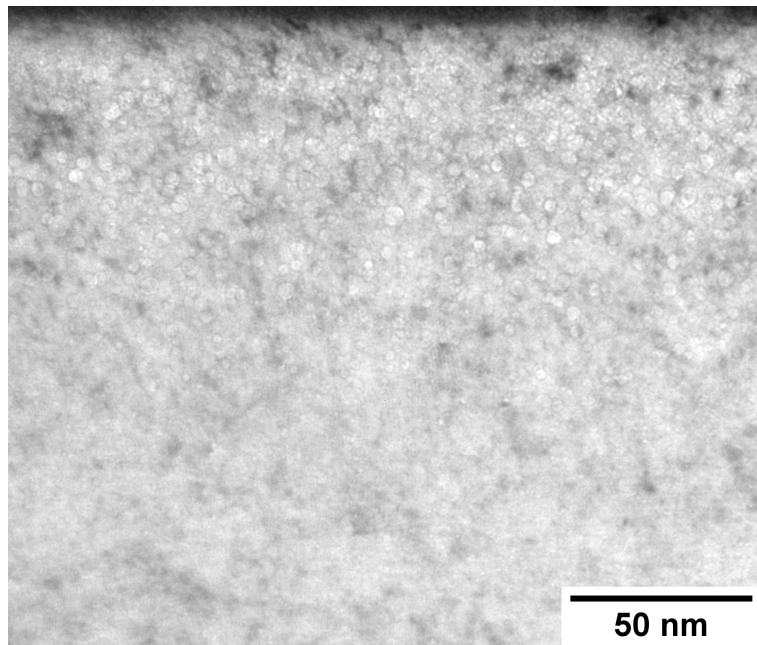


Figure 2.29: 97kx resolution of He+Fe lamella.

## 2.8.3 Analysis in ImageJ

The images produced in the TEM were analyzed using ImageJ. ImageJ is a Java based open source application used for measurement and analysis of microscopic images. ImageJ maintains the pixel to nanometer scale from the TEM images and comes with a suite of tools for image editing and measuring regions of interest.

For each lamella a 97kx resolution image was used for analysis. Each image was cropped such that the platinum layer was excluded from the image. The edge of steel sample marked 0

nm as shown in Figure 2.30. The helium bubbles presented themselves as a pale circles with dark outer rings when the underfocused images were used and as dark circles with pale edges in the overfocused images.

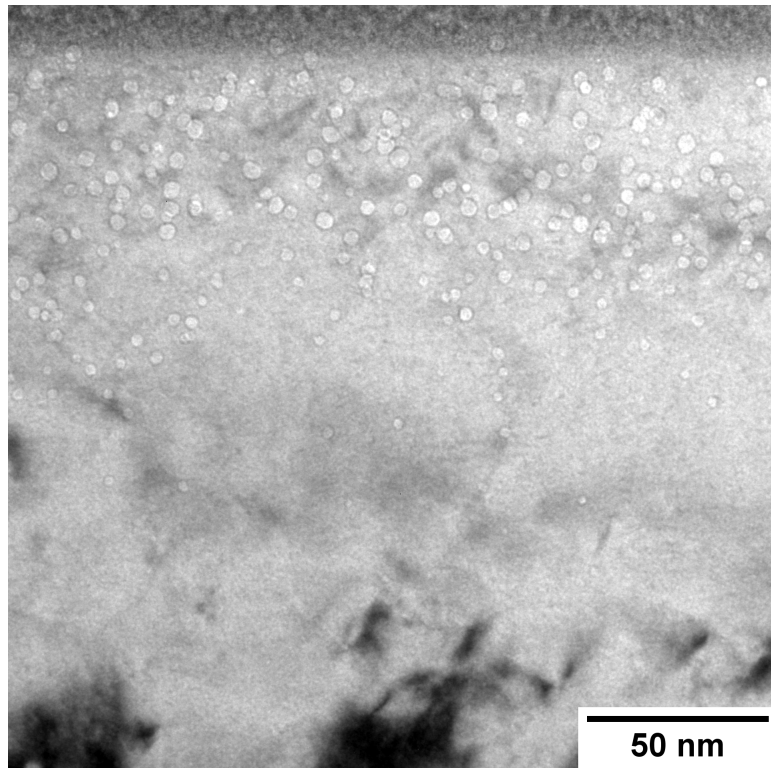


Figure 2.30: 97kx TEM image of  $3E16$  He implantation.

Using the ellipse selection tool each bubble was fitted with a ring that matched its perimeter as closely as possible. The area inside this ring was then filled with a bright red color and measured using ImageJ's built in measurement tool. Figure 2.31 shows a section of the sample before and after measurement and marking had taken place. The measurement tool captured not only the cross-sectional area of the bubble but the coordinates of the center as well.

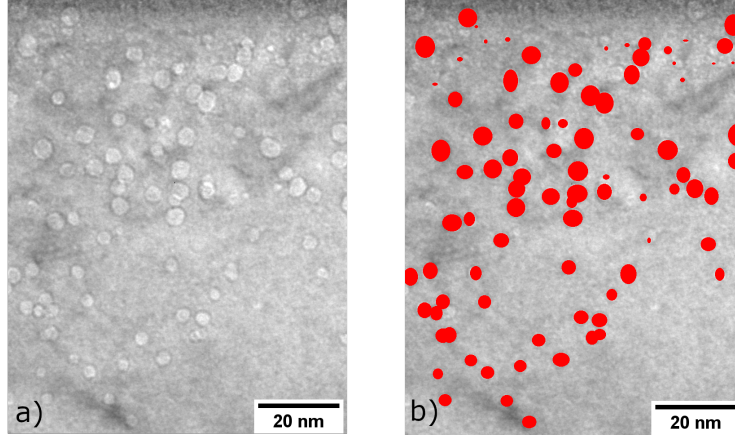


Figure 2.31: Sample image a) before and b) after bubble marking and measurement.

#### 2.8.4 Bubble Concentration

The area of each bubble was used to find equivalent radii and volumes. The center measurements were then used to plot bubble radius against depth in the target. The distribution of bubbles in a 150 nm depth was also plotted for all four lamella. This distribution was achieved by creating a histogram with bins set at 3 nm intervals. The y-coordinates were used to create a tally  $N_{He}$  and an average radius  $\bar{r}$  was found for each 3 nm section of each sample using Equation 2.13.

$$\bar{r} = \frac{\sum r_i}{N_{He}} \quad (2.13)$$

The standard deviation of each average radius was also calculated to illustrate the variance in bubble size at each depth in the target. The standard deviation  $\sigma_r$  was calculated with Equation 2.14

$$\sigma_r = \sqrt{\frac{\sum (r_i - \bar{r})^2}{N_{He}}} \quad (2.14)$$

### 3. RESULTS AND DISCUSSION

#### 3.1 Ion Identification

Table 3.1: Results of magnet scans.

Peak	Potential Ion	I <sub>1</sub> (A)	I:I <sub>He<sup>+</sup>,1</sub>	I <sub>2</sub> (A)	I:I <sub>He<sup>+</sup>,2</sub>	I <sub>3</sub> (A)	I:I <sub>He<sup>+</sup>,3</sub>	I <sub>4</sub> (A)	I:I <sub>He<sup>+</sup>,4</sub>
1	H <sup>+</sup>	0.20	0.4	0.20	0.5	0.19	0.463	0.19	0.463
2	He <sup>2+</sup> , D	0.30	0.6	0.30	0.75	0.28	0.683	0.28	0.683
3	He <sup>+</sup>	0.50	1	0.40	1	0.41	1	.041	1
4	Li <sup>+</sup> , N <sup>+</sup> , CO <sup>2+</sup>	0.65	1.3	0.60	1.5	0.75	1.829	-	-
5	S <sup>2+</sup> , O <sup>+</sup> , H <sub>2</sub> O <sup>+</sup> ,	1.05	2.1	0.85	2.13	-	-	-	-
6	Na <sup>+</sup> , CO <sub>2</sub> <sup>+</sup> , Fe <sup>2+</sup> ,	1.20	2.4	1.00	2.5	0.95	2.317	-	-
7	Ca <sup>+</sup> , CO <sub>2</sub> <sup>+</sup> , Fe <sup>+</sup>	1.80	3.6	1.40	3.5	1.40	3.415	-	-

The results of the four magnet scans are found in Table 3.1. The results show that as the scans progressed the magnet current associated with each peak shifted slightly towards a final value. This effect was attributed to lingering hysteresis effects from the magnet being run in the opposite direction prior to being used in this assembly.

In the first two sets of scans the first three peaks were identified as H<sup>+</sup>, He<sup>2+</sup> (D), and He<sup>+</sup>. Due to the magnetic field for deuterium and He<sup>2+</sup> being within 0.2% of each other and the limited distance from the bending magnet to the collection plate this system was unable to resolve the currents from doubled charged helium and deuterium. The fourth peak had the potential to be Li<sup>+</sup> or N<sup>2+</sup> which had current ratios of 1.317 or 1.323 respectively on Table A.1. Peak 5 could be interpreted as S<sup>2+</sup> (2.001), O<sup>+</sup> (1.999), or H<sub>2</sub>O<sup>+</sup> (2.1). Peak 6 was close to Fe<sup>2+</sup>, Na<sup>+</sup>, and CO<sub>2</sub><sup>+</sup>. Peak 7 was closest to Ca<sup>+</sup>, Fe<sup>+</sup>, and CO<sub>2</sub><sup>+</sup>. Each batch of potential ion species was plotted in Figures 3.1-3.3. A linear regression was applied to each data set and the R<sup>2</sup> was used to determine the measure of accuracy in each set. It was determined that Figure 3.1 was the correct B-I curve. These currents were then used in all subsequent experiments.

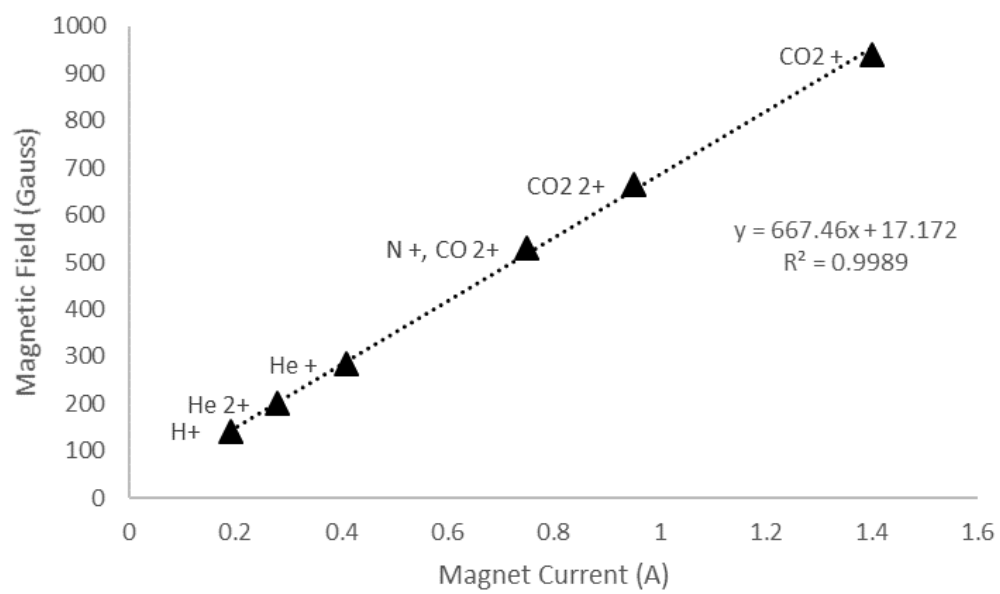


Figure 3.1:  $H^+$ ,  $He^{2+}$ (D),  $He^+$ ,  $Li^+$ ,  $N^+$ ( $CO^{2+}$ ),  $CO_2^{+,2+}$ .



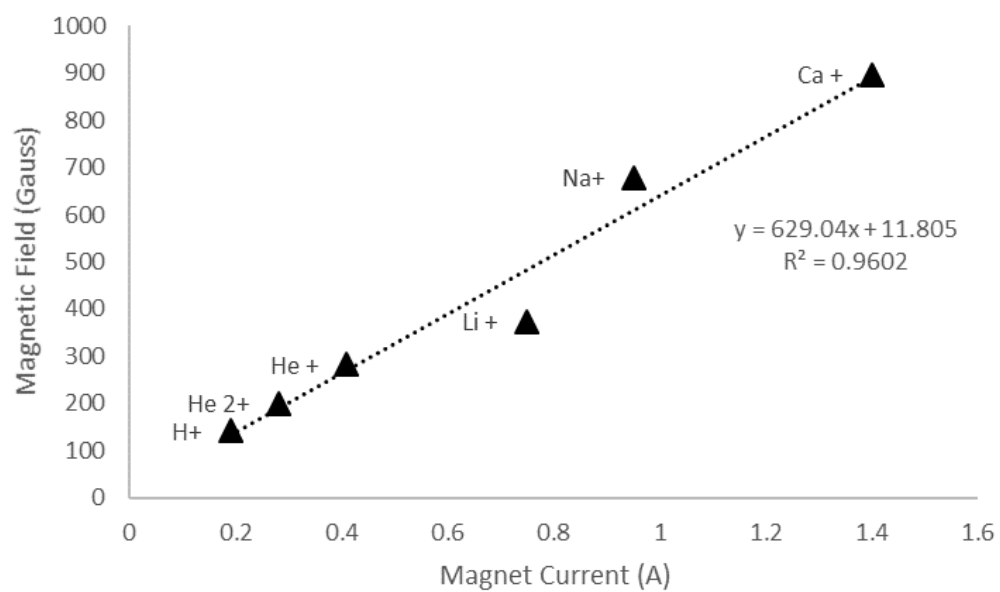


Figure 3.2: B-I curve for H<sup>+</sup>, He<sup>2+</sup>(D), He<sup>+</sup>, Li<sup>+</sup>, Na<sup>+</sup>, Ca<sup>+</sup>.

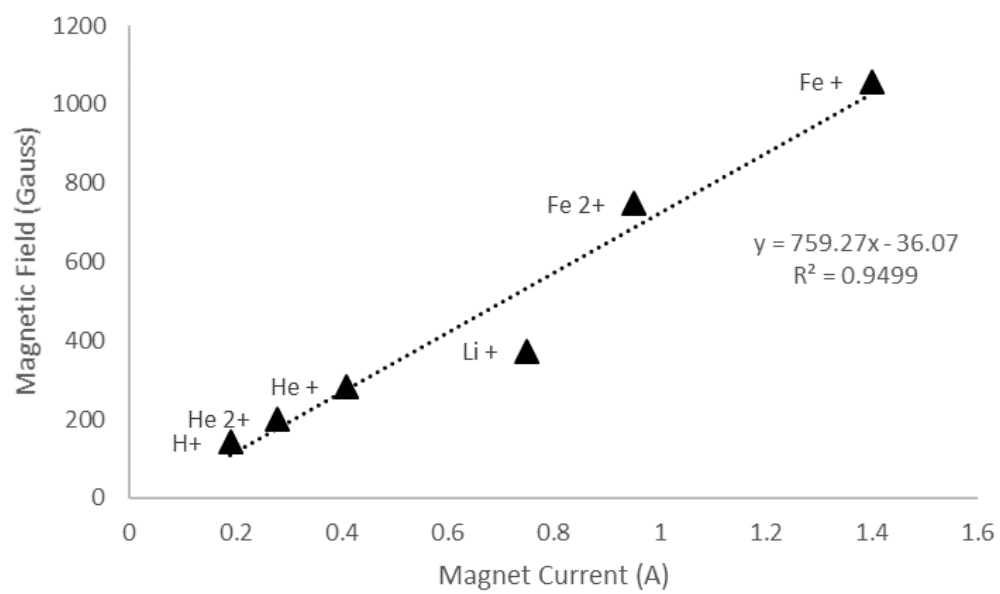


Figure 3.3: B-I curve for H<sup>+</sup>, He<sup>2+</sup>(D), He<sup>+</sup>, Li<sup>+</sup>, Fe<sup>+</sup>, Fe<sup>2+</sup>.

### 3.2 10 keV He<sup>+</sup> into Stainless Steel

The initial helium only implantation shown in Figure 3.4 served as a benchmark for the helium deposited by the 10 kV accelerator. In Figure 3.5 a maximum depth of approximately 150 nm can be seen for bubble formation, while the majority of the bubble formation resides in the 40-50 nm range. This fell in line with ranges found in SRIM simulations. Figure 3.5 illustrated the need for an extremely thin lamella. In this image it was impossible to tell if bubbles had been stacked on top of each other. Subsequent lamella in the dual beam experiments were thinned down to a range of 100 nm or smaller to reveal only a single layer of bubbles.

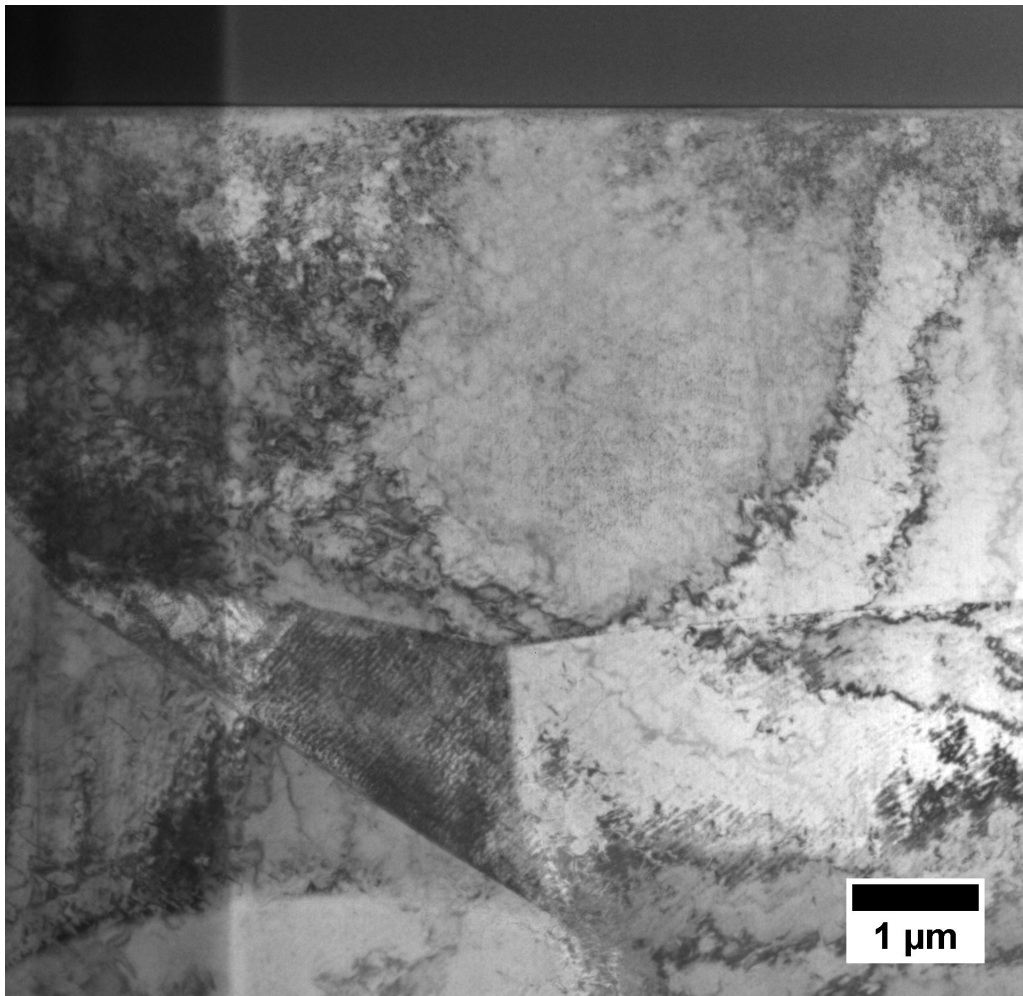


Figure 3.4: Stainless steel after  $8 \cdot 10^{16}$  ions·cm<sup>-2</sup> He<sup>+</sup> dose.

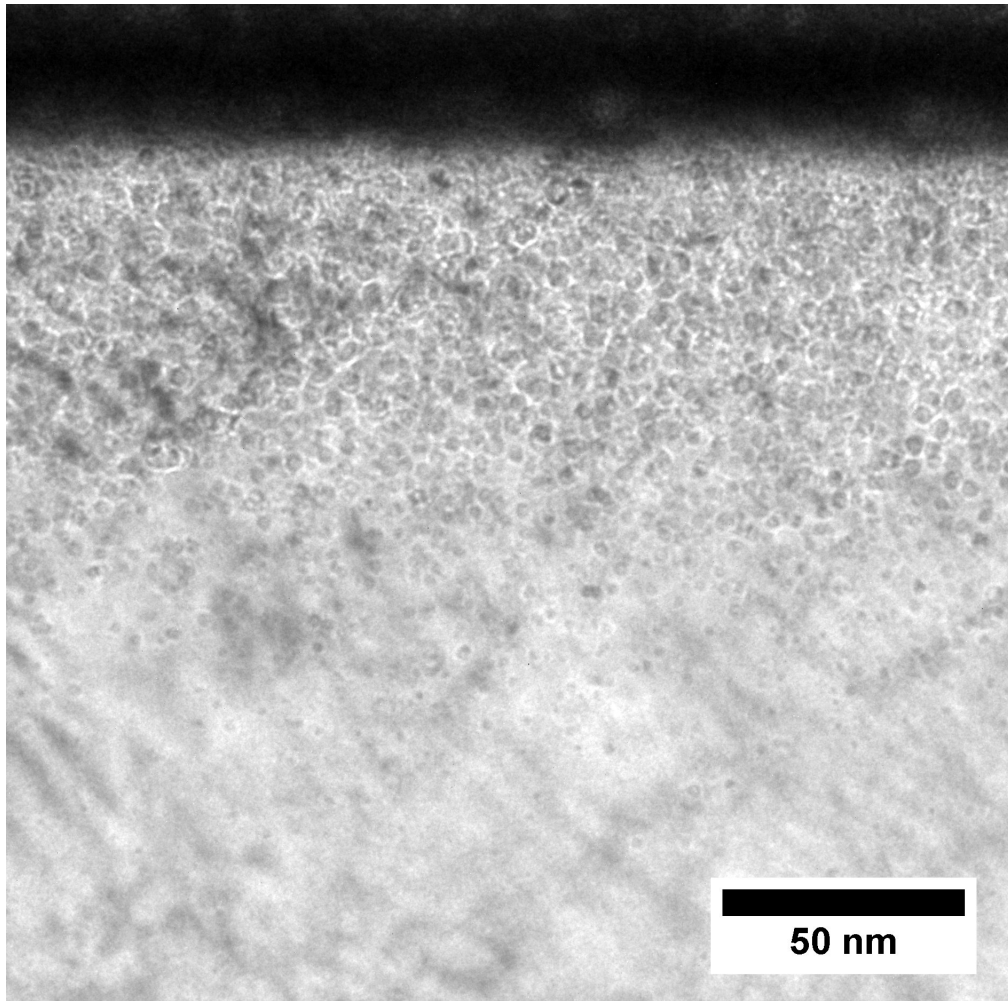


Figure 3.5: 97kx magnification of stainless steel after  $8 \cdot 10^{16}$  ions·cm<sup>-2</sup> He<sup>+</sup> dose.

### **3.3 He vs. Fe+He Implantation**

The bubble measurements taken from all four sample regions of the single and dual beam implantations showed a consistent pattern. In the samples where iron was implanted simultaneously there is a significant increase in nucleation sites for helium bubbles. Conversely because the same amount of helium was implanted across both He and Fe+He samples the average bubble size at a given depth in the target was consistently smaller in the Fe+He samples.

#### **3.3.1 Deposition of He Across Samples**

To ensure both regions of interest in each dose were uniformly implanted with helium the total bubble volume by depth in the target was examined. In Figures 3.6 and 3.7 the volume content in both regions were extremely close fitting. This indicates that despite the difference in bubble sizes roughly the same amount of helium was present in both sets of samples.

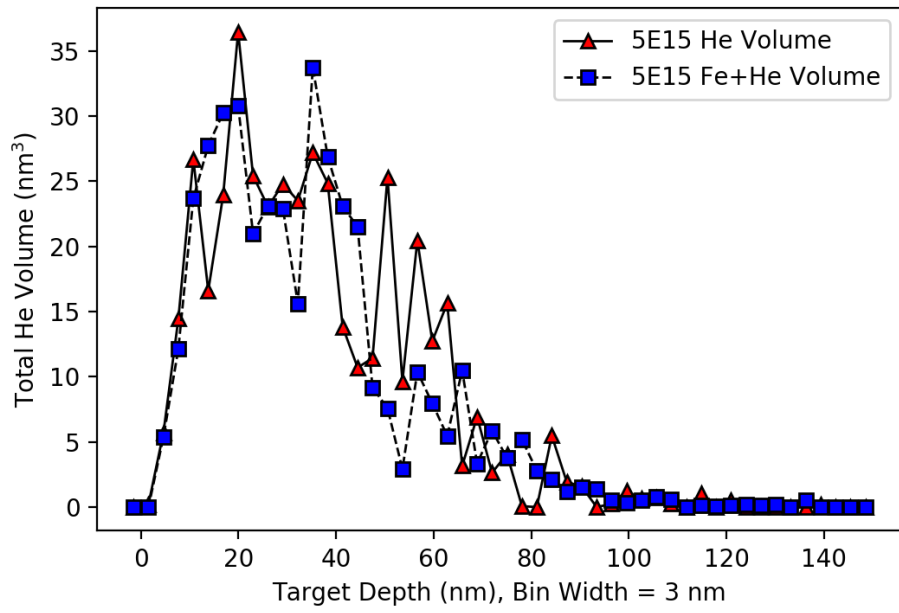


Figure 3.6: Total volume of helium by depth for  $5.0 \cdot 10^{15}$  ions·cm<sup>-2</sup>.

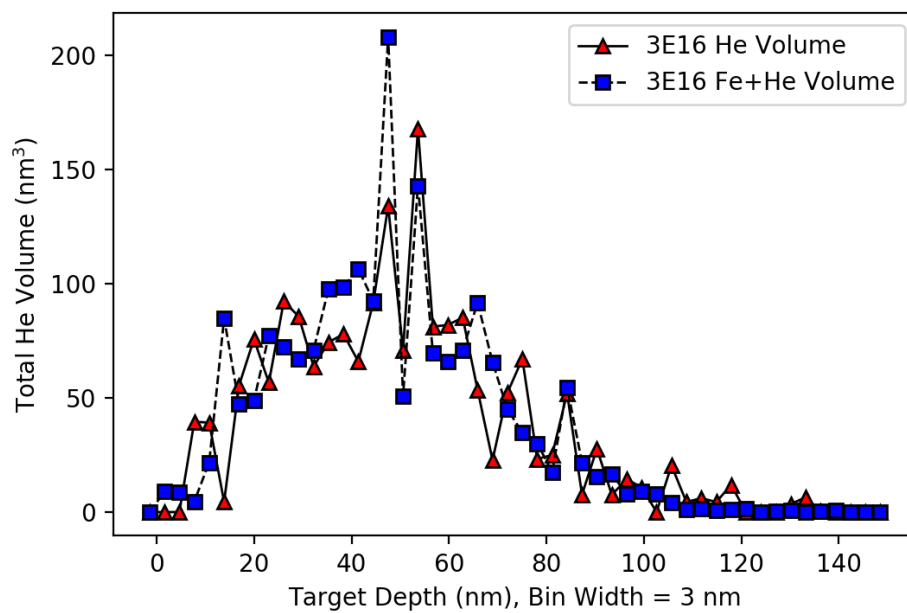


Figure 3.7: Total volume of helium by depth for  $3.0 \cdot 10^{16}$  ions·cm<sup>-2</sup>.

### 3.3.2 $5 \cdot 10^{15} \Phi$ Irradiation of 316L

In the  $5.0 \cdot 10^{15} \text{ ions} \cdot \text{cm}^{-2}$  experiment Figures 3.8 and 3.9 were compared and increased number of bubbles was seen forming with a radius close to the 0.3 nm range. In Figure 3.11 the overall bubble count by depth was significantly increased with the addition of iron. Also in Figure 3.11 it was observed that this increased damage from iron allowed more nucleation sites a greater depths into the target. The difference in average bubble radii in Figure 3.10 between He and He+Fe was as large as 1 nm.

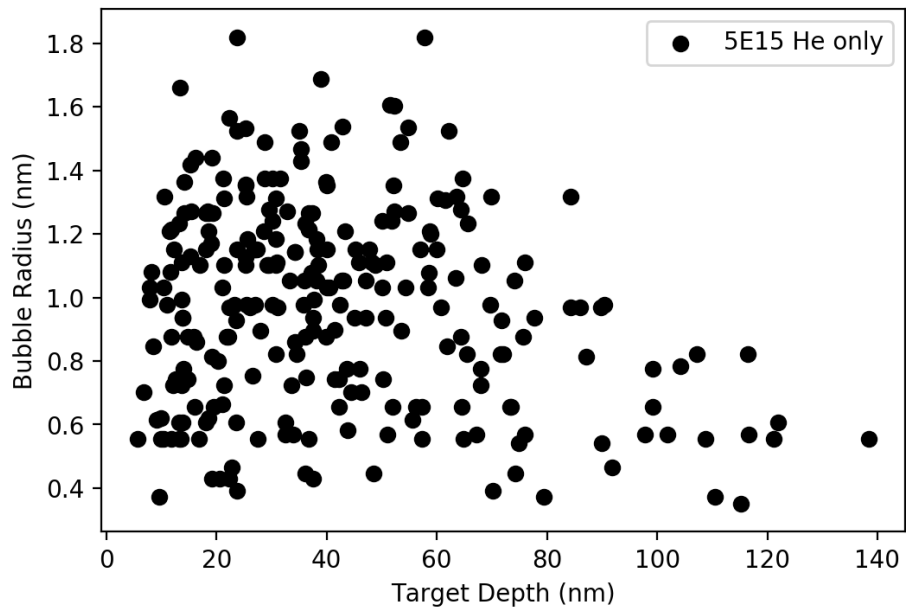


Figure 3.8: Bubble radius by depth for  $5.0 \cdot 10^{15} \text{ ions} \cdot \text{cm}^{-2}$  He.



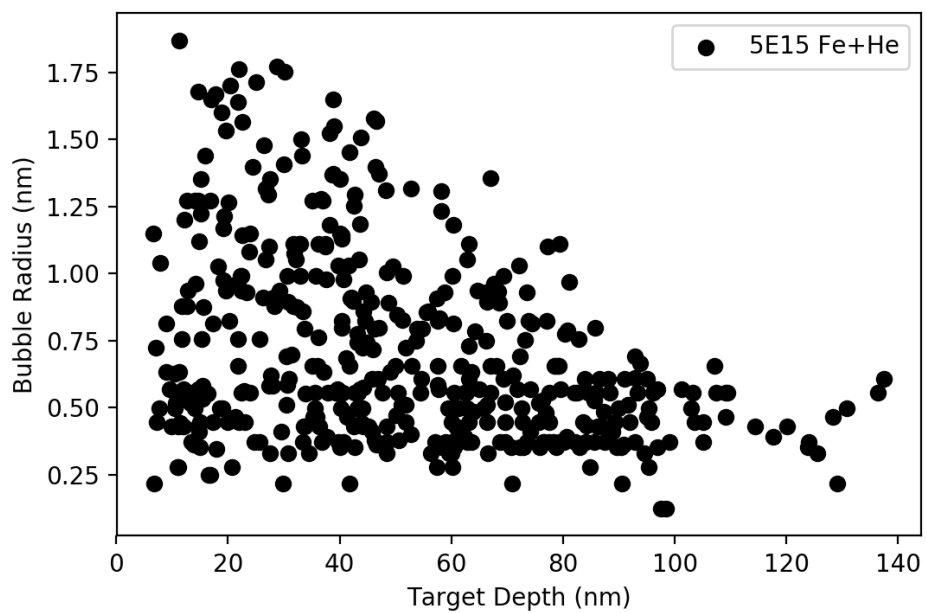


Figure 3.9: Bubble radius by depth for  $5.0 \cdot 10^{15}$  ions $\cdot$ cm $^{-2}$  He+Fe.

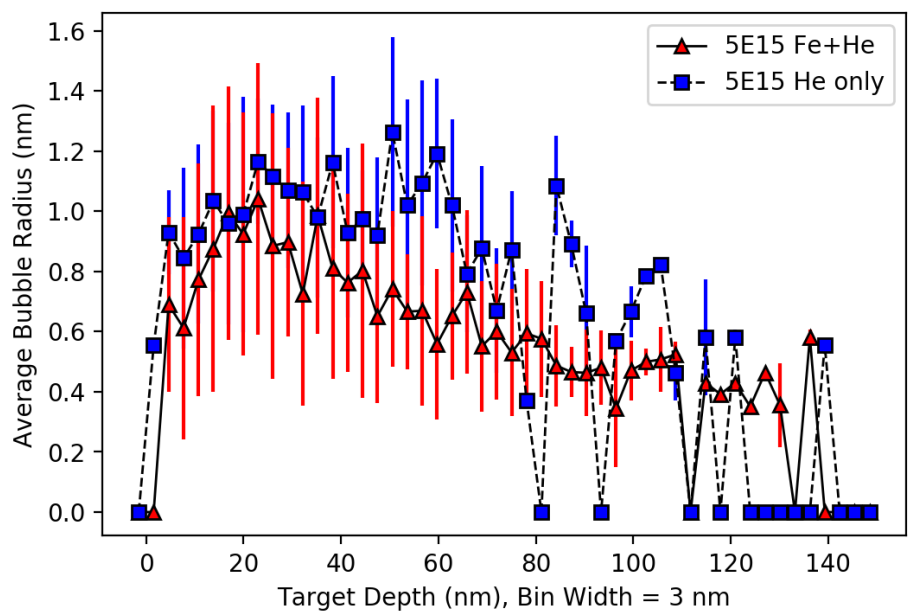


Figure 3.10: Average bubble formation size for  $5.0 \cdot 10^{15}$  ions·cm<sup>-2</sup> He & He+Fe.

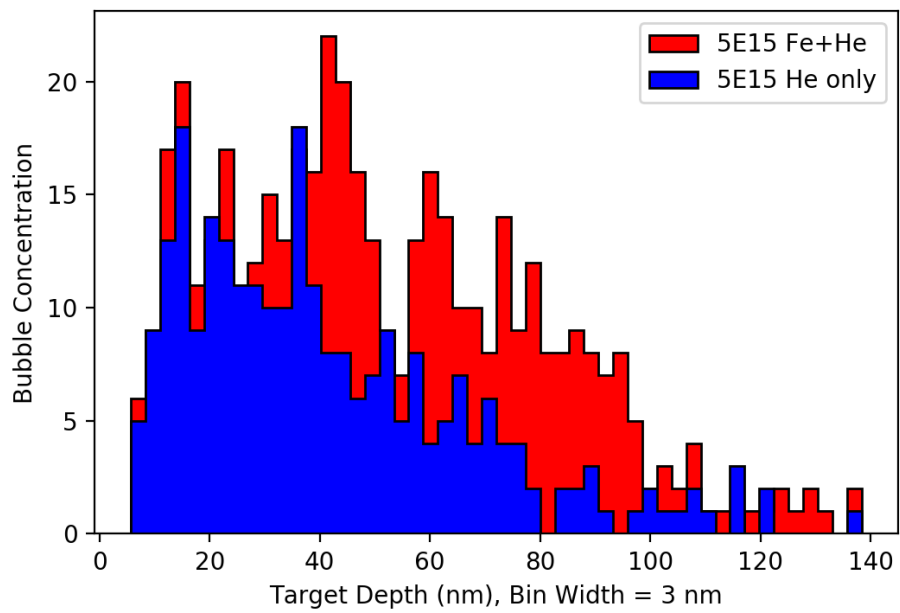


Figure 3.11: Bubble concentration by depth for  $5.0 \cdot 10^{15}$  ions·cm<sup>-2</sup> He & He+Fe.

### 3.3.3 $3 \cdot 10^{16} \Phi$ Irradiation of 316L

In the higher fluence study the effect of iron on bubble formation was more pronounced. From depths 0-60 nm and 70-150 nm Figures 3.12-3.15 showed a decreased average radius and increased bubble nucleation than was seen in the  $5.0 \cdot 10^{15}$  (ions $\cdot$ cm $^{-2}$ ) sample. However an interesting effect was observed in the 60-70 nm region. In this range the average bubble size and concentration between the He and He+Fe samples are nearly identical. In this area it seemed that the helium was reaching an equilibrium point by combining smaller bubbles into larger ones.

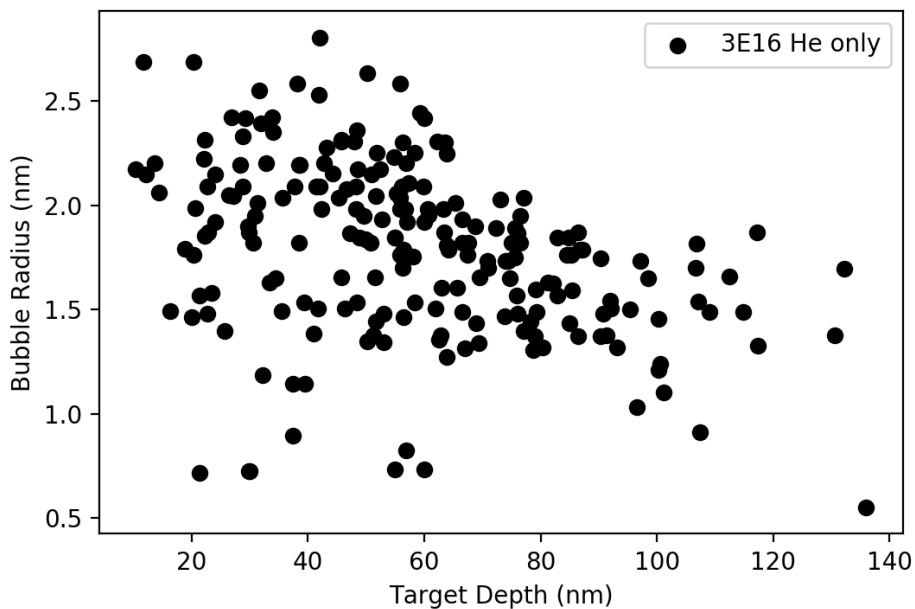


Figure 3.12: Bubble radius by depth for  $3.0 \cdot 10^{16}$  ions $\cdot$ cm $^{-2}$  He.

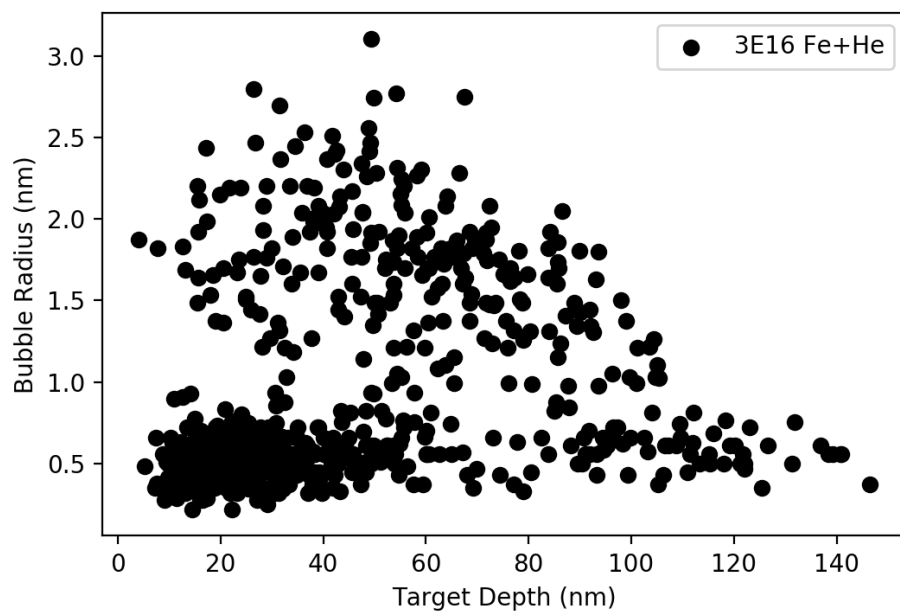


Figure 3.13: Bubble radius by depth for  $3.0 \cdot 10^{16}$  ions·cm<sup>-2</sup> He+Fe.

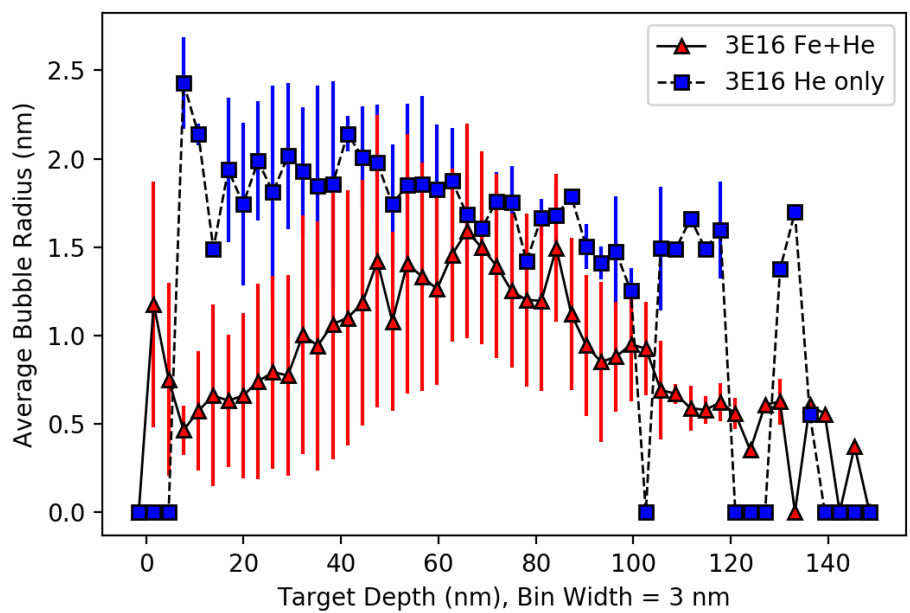


Figure 3.14: Average bubble formation size for  $3.0 \cdot 10^{16}$  ions·cm<sup>-2</sup> He & He+Fe.

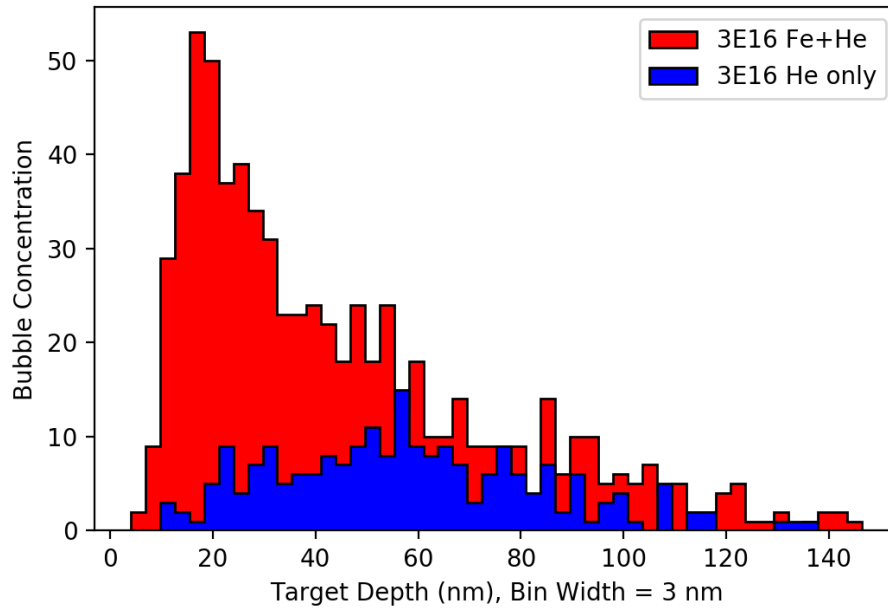


Figure 3.15: Bubble concentration by depth for  $3.0 \cdot 10^{16}$  ions·cm<sup>-2</sup> He & He+Fe.

### 3.3.4 Temperature Study

To ensure the additional nucleation was not due to an increased sample temperature from the beam deposition a thermal model was built in ANSYS. The model shown in Figure 3.16 assumed only a radiative heat transfer on the five faces not attached to the stage. Since there was a large difference between the bulk sample thickness and the deposition depth of the ions each beam was treated as a surface flux of incoming heat. The results of the model show that there was a 1% difference in temperature between the two irradiation spots. With such a marginal difference increased vacancies due to thermal expansion were disregarded.

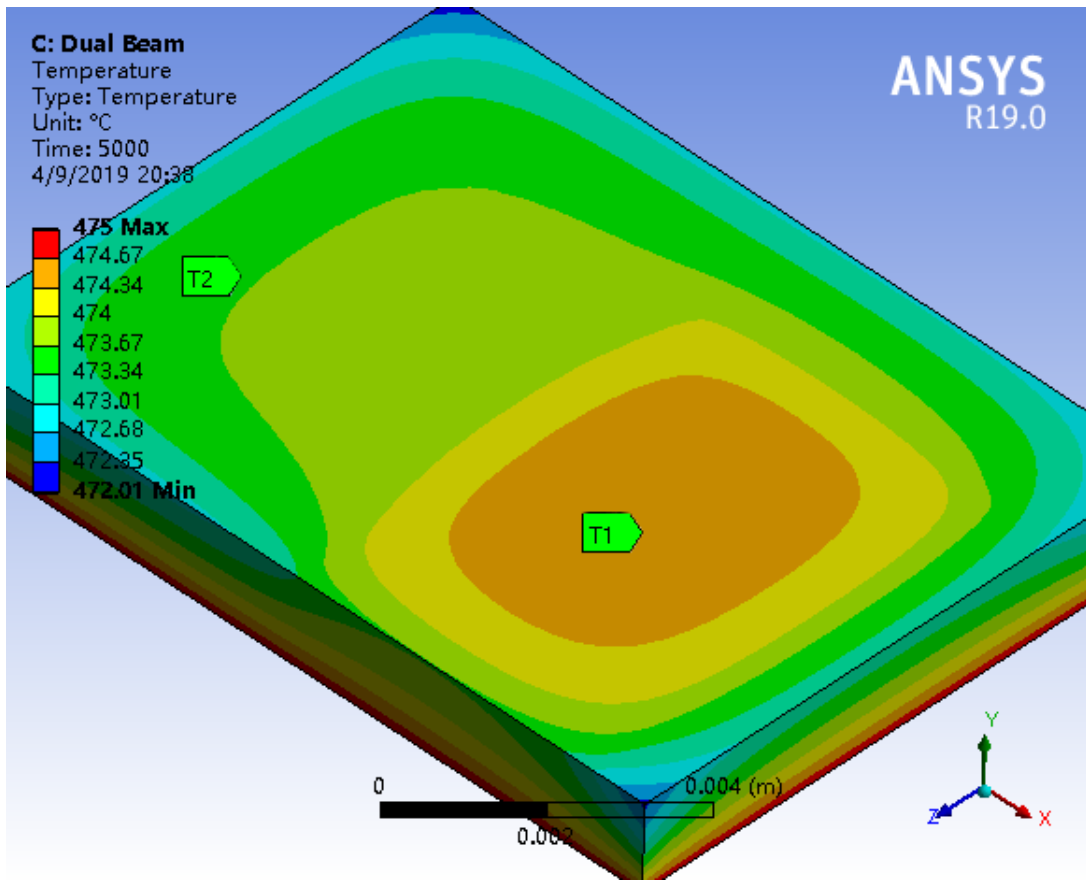


Figure 3.16: ANSYS thermal study of surface temperature distribution.



## 4. CONCLUSION

If perfected fusion reactor technology has the potential to be the cleanest most abundant energy source possible. Examination of the effects of fusion like environments on materials used in shielding and equipment in fusions reactors will help engineers and scientists understand the challenges faced when designing, constructing, and operating such a reactor.

In this thesis a 10 kV accelerator was successfully rebuilt and attached to a 1.7 MV Tandem accelerator with the purpose of simulating multiple incident ions. The experiment was able to successfully implant two unique ion species in the same target simultaneously. A half & half approach was used in implantation that drastically cut down the time and difficulty required to generate two samples with an identical helium deposition and one with an additional iron implantation. Examination of the total helium content in the samples confirmed the helium deposition was evenly performed across both samples. The two separate fluences illustrated the dependence on dose of helium bubble formation.

The introduction of additional damage from iron ions increased the total number of bubble nucleation sites within the first 150 nm of the target samples in both the  $5.0 \cdot 10^{15}$  ions $\cdot$ cm $^{-2}$  and  $3.0 \cdot 10^{16}$  ions $\cdot$ cm $^{-2}$  doses. A comparison of bubbles formed with the addition of ion showed that the average bubble size was reduced when more nucleation sites were present. A thermal model of the experimental parameters ruled out additional vacancies due to increased surface temperature from iron deposition.

While this experiment used a self implantation with iron, the method used in this experiment could be used in a great number of additional studies. This same dual beam experiment can be applied to several combinations of helium and high energy hydrogen implantations. This system could also possibly be used to determine a saturation point where the effects of iron damage will be negligible in comparison to the helium bubbles.

## REFERENCES

- [1] A. Lépine-Szily and P. Descouvemont, “Nuclear astrophysics: Nucleosynthesis in the Universe,” *International Journal of Astrobiology*, vol. 11, pp. 243–250, 10 2012.
- [2] K. Miyamoto, *Plasma Physics and Controlled Nuclear Fusion*. Springer series on atomic, optical, and plasma physics: 38, Berlin ; New York : Springer, [2005], 2005.
- [3] S. Li, H. Jiang, Z. Ren, C. Xu , “Optimal Tracking for a Divergent-Type Parabolic PDE System in Current Profile Control,” *Abstract and Applied Analysis*, vol. 2014, no. 940965, 2014.
- [4] D. S. Darrow, S. J. Zweben, S. Batha, R. V. Budny, C. E. Bush, Z. Chang, C. Z. Cheng, H. H. Duong, J. Fang, N. J. Fisch, R. Fischer, E. D. Fredrickson, G. Y. Fu, R. F. Heeter, W. W. Heidbrink, H. W. Herrmann, M. C. Herrmann, K. Hill, E. F. Jaeger, R. James, R. Majeski, S. S. Medley, M. Murakami, M. Petrov, C. K. Phillips, M. H. Redi, E. Ruskov, D. A. Spong, E. J. Strait, G. Taylor, R. B. White, J. R. Wilson, K. Wong, and M. C. Zarnstorff, “Alpha particle losses from tokamak fusion test reactor deuterium–tritium plasmas,” *Physics of Plasmas*, vol. 3, no. 5, pp. 1875–1880, 1996.
- [5] Peixuan Wang, Yupu Li, Jiarui Liu , Guoguang Zhang , Ruzhang Ma, Peiruan Zhu, Changqing Qiu and Tianbing Xu , “A study of helium trapping, bubble structures and helium migration in type 316l stainless steel under helium implantation,” *Journal of Nuclear Materials*, vol. 169, pp. 167–176, 1989.
- [6] M.J. Baldwin and R.P. Doerner, “Helium induced nanoscopic morphology on tungsten under fusion relevant plasma conditions,” *Nuclear Fusion*, vol. 48, p. 035001, Jan. 2008.
- [7] Dai Nishijima, M.Y. Ye and Noriyasu Ohno, Shuichi Takamura , “Formation mechanism of bubbles and holes on tungsten surface with low-energy and high-flux helium plasma irradiation in nagdis-ii,” *Journal of Nuclear Materials*, vol. 329-333, pp. 1029–1033, August 2004.

- [8] Y. Ueda, M. Fukumoto, J. Yoshida, Y. Ohtsuka, R. Akiyoshi, H. Iwakiri, N. Yoshida , “Simultaneous irradiation effects of hydrogen and helium ions on tungsten,” *Journal of Nuclear Materials*, vol. 386-388, no. 51, pp. 725–728, 2009.
- [9] Erik Wahlin, “Model 200-B Lens Schematic.” Drafted schematic.
- [10] A.A. Harms, K.F. Schoepf, G.H. Miley, D.R. Kingdon, *Principles of Fusion Energy*. World Scientific Publications.
- [11] Oliphant, Mark; Harteck, Paul; Rutherford, Ernest , “Transmutation effects observed with heavy hydrogen,” *Proceedings of the Royal Society*, vol. 144, no. 853, pp. 692–703, 1934.
- [12] M. Kikuchi, K. Lackner & M. Q. Tran, *Fusion Physics*. International Atomic Agency, 2012.
- [13] R. M. Mayo, *Introduction to Nuclear Concepts For Engineers*. La Grange Park, Ill., USA : American Nuclear Society, [1998], 1998.
- [14] Gary S. Was, *Fundamentals of Radiation Materials Science*. Springer, 2007.
- [15] A. Septier, *Focusing of Charged Particles, Vol. I*. New York : Academic Press, 1967-, 1967.
- [16] A. Septier, *Focusing of Charged Particles, Vol. II*. New York : Academic Press, 1967-, 1967.
- [17] S. Lee, *Accelerator Physics, Second Edition*. World Scientific, 2004.
- [18] “Atomic Weights and Isotopic Compositions with Relative Atomic Masses.” <https://www.nist.gov/pml/atomic-weights-and-isotopic-compositions-relative-atomic-masses>. Accessed: 2019-02-12.
- [19] Soshin Chikazumi, *Physics of Ferromagnetism*. Oxford Science Publications, 1997.
- [20] High Voltage Engineering Corp., “998-2 Schmeatics.” Drafted schematic.

APPENDIX A

DATA

Table A.1: Magnetic fields required for ions bending at a 1.016 m radius.

Species	Mass (amu)	$X^+$		$X^{2+}$	
		B (Gauss)	$B:B_{He^+}$	B (Gauss)	$B:B_{He^+}$
H	1.008	142.191	0.502	-	-
D	2.014	200.966	.709	-	-
T	3.016	245.928	0.868	-	-
He	4.003	283.311	1.000	200.331	0.707
Li	6.942	373.117	1.317	263.833	0.931
Be	9.012	425.115	1.501	300.602	1.061
B	10.812	465.641	1.644	329.258	1.162
C	12.011	490.779	1.732	347.033	1.225
N	14.007	529.990	1.871	374.760	1.323
O	15.999	566.424	1.999	400.522	1.414
H <sub>2</sub> O	18.016	601.059	2.122	425.013	1.500
Na	22.990	678.983	2.397	480.113	1.695
CO	28.010	749.466	2.645	529.953	1.871
Si	28.085	750.469	2.649	530.661	1.873
Ar	39.948	895.034	3.159	632.885	2.234
CO <sub>2</sub>	44.010	939.433	3.316	664.280	2.345
Fe	55.845	1058.241	3.735	748.289	2.641

# APPENDIX B

## SCHEMATICS

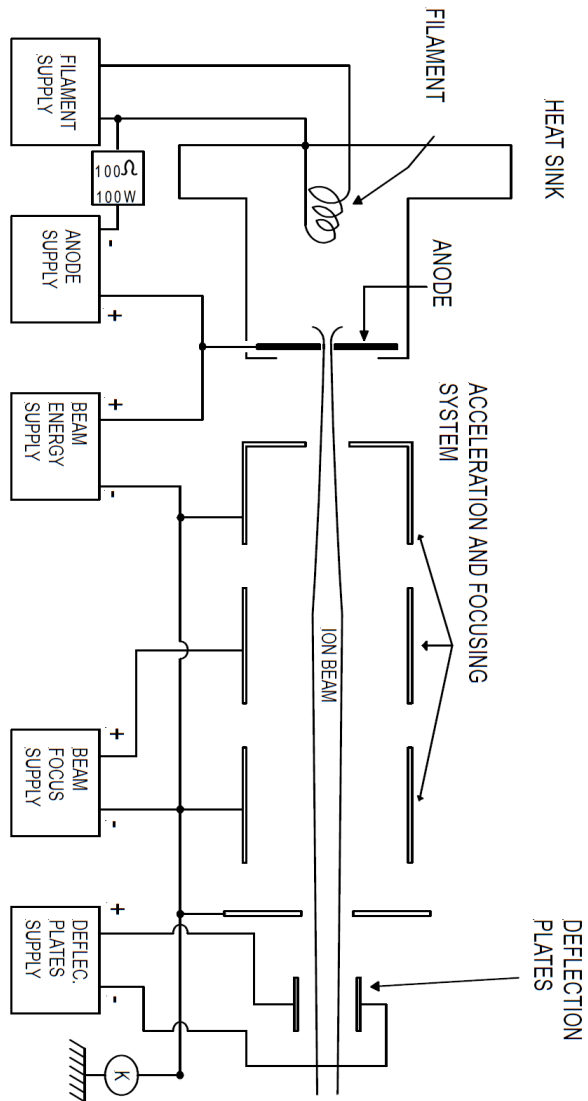


Figure B.1: Colutron DC ion source schematic. Adapted from *Wahlin 2018* [9].

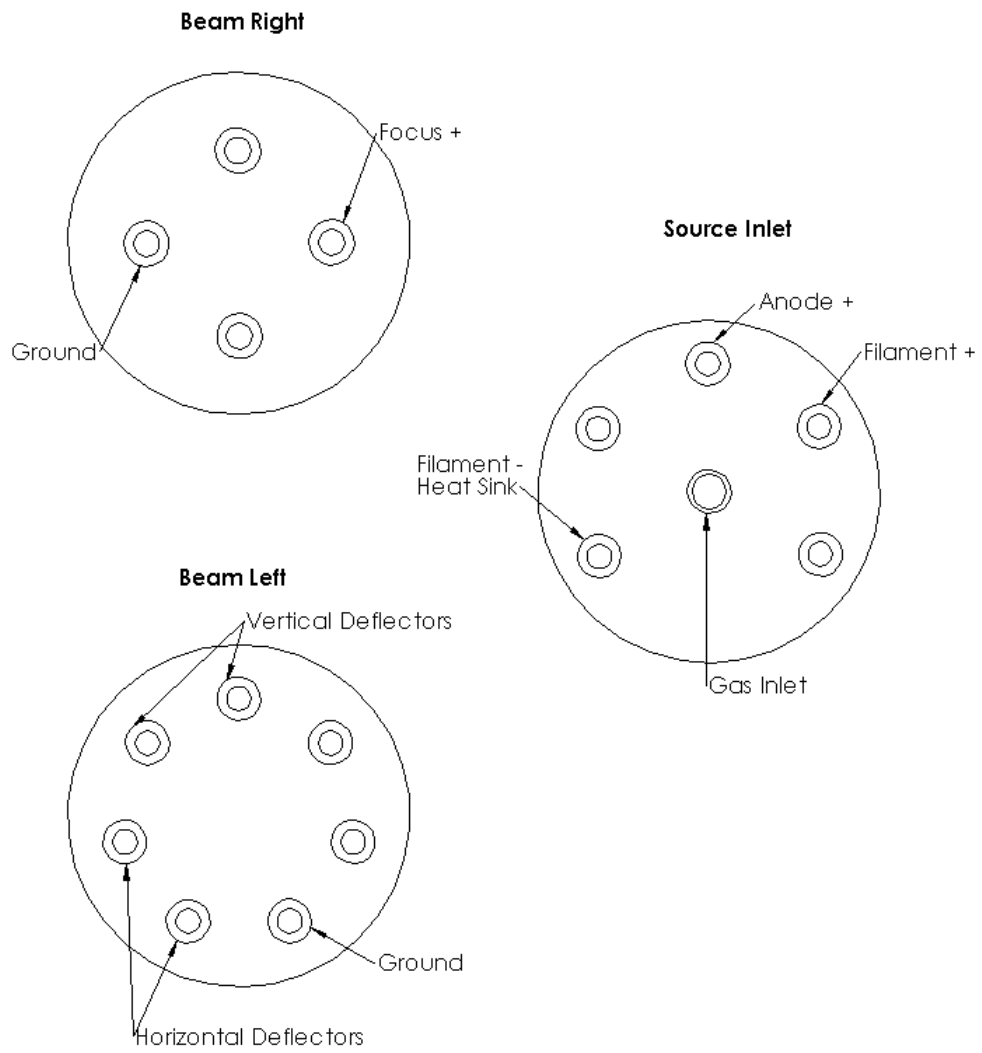


Figure B.2: Electrical input flange schematics.

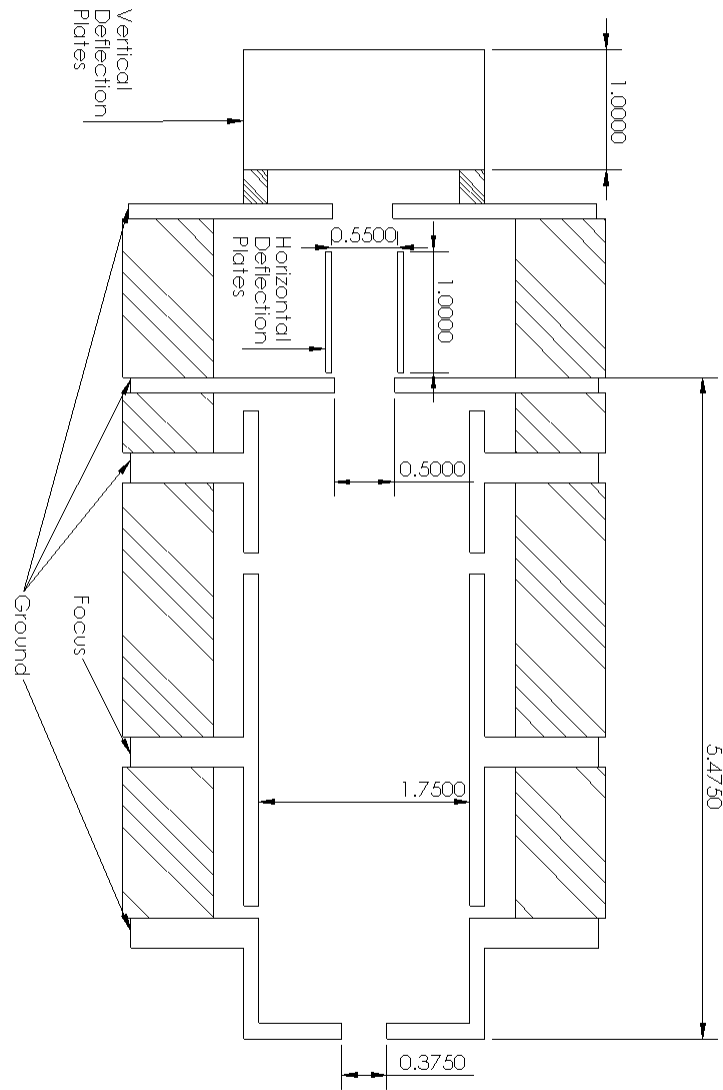


Figure B.3: Colutron 200-B lens system, dimensions in inches. Adapted from *Wahlin 2018*[9].

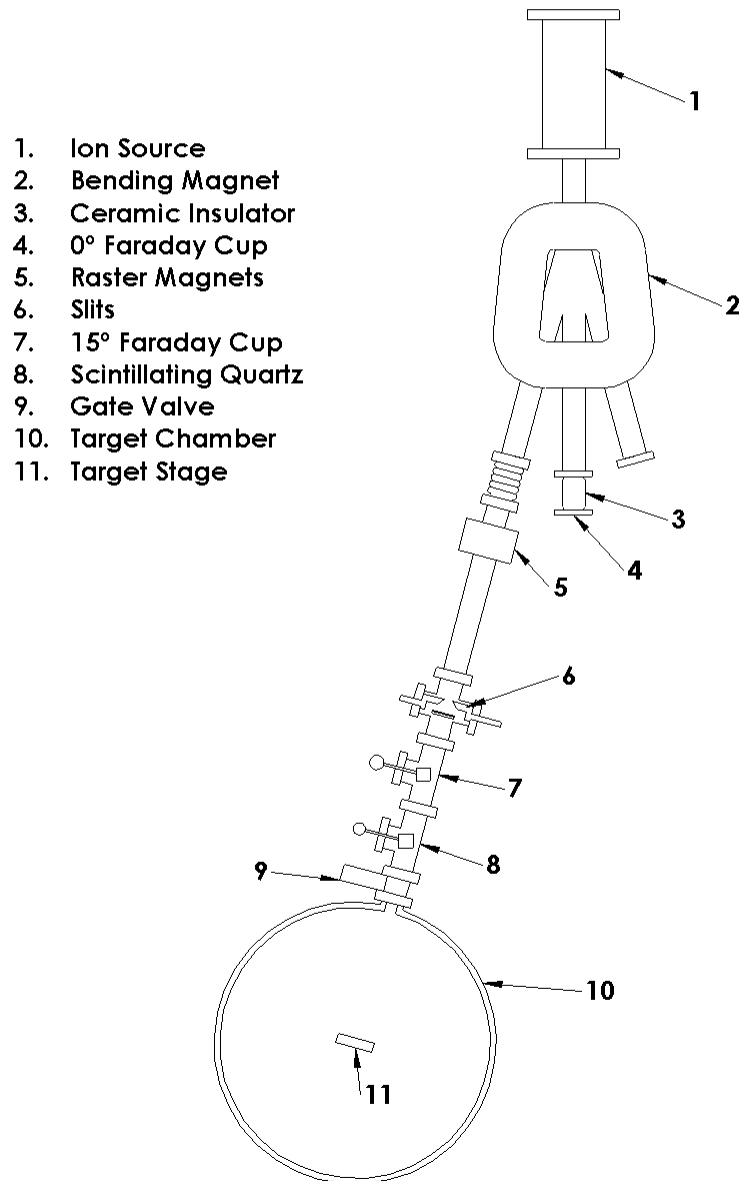
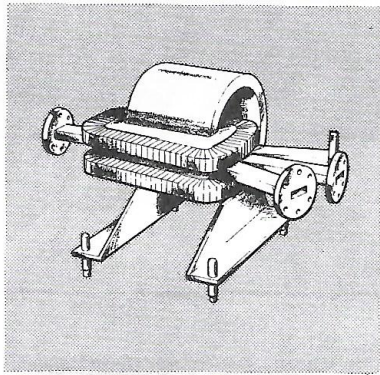


Figure B.4: 10 keV Beamline schematic.

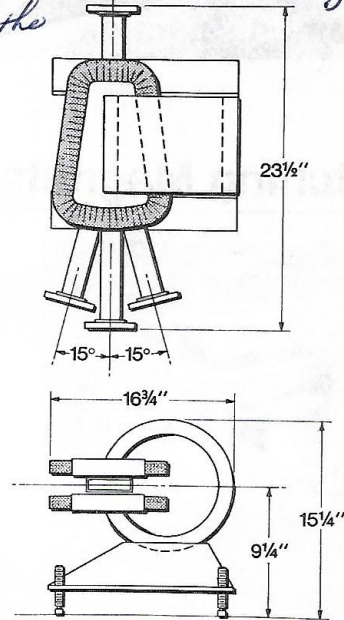




PART NO. 998-2

*Dimension would suggest it is this one, but this one up at least in the picture has only 2 coils & is air cooled only. That could change the B-I curve*

- Analyzer and Switching
- Complete with Power Supply and Controls
- Double Focusing
- For use with Low Energy Beams
- Low Cost



**MAGNET**

Air Gap .....	0.94 inches
Field (Maximum) .....	2900 gauss
Radius of Curvature at 15° .....	40 inches
Deflection Angles .....	±15°/0°
Residual Field .....	22 gauss
Weight .....	240 pounds

**CHAMBER**

Waveguide .....	.75 x 1.5 x .06
Cooling .....	Air

**COILS**

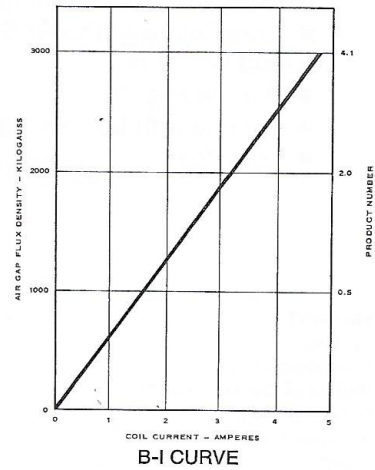
Type .....	wire
Turns per Coil .....	1,150
Cooling .....	Air

**MOUNT**

Vertical Adjustment .....	±1.0 inch
---------------------------	-----------

**POWER SUPPLY**

.....	80V, 5a
Line and Load Regulation .....	±0.75% or ±20 mV
Current Stability .....	12 mv per °C



**ORDERING INFORMATION**

Please address orders to Equipment Division, High Voltage Engineering Corporation, Burlington, Massachusetts 01803. When ordering please specify part number, description and size. For prices, refer to the current HVE price list. Contact your nearest sales office for additional information.

Main office and plant: South Bedford Street, Burlington, Massachusetts 01803, Telephone: 617-272-1313, Cable HIVOLT TWX 710-332-0245.

Mid-Western regional office: 7710 Carondelet Avenue, St. Louis, Missouri 63105. Telephone: 314-863-3311.

Western regional office: 703 Welch Road, Suite F-1, Palo Alto, California 94304, Telephone: 415-328-2181.

European sales office: Amsterdamseweg 61, Amersfoort, Holland, Telephone: (03490) 19741, Telegram: EUROVOLT TELEX 47275.

Figure B.5: Bending magnet dimensions and properties. Adapted from HVE 2018 [20].

## APPENDIX C

### PYTHON CODE

```
## Loads the numerical and plotting packages used
import numpy as np
from scipy import stats
import matplotlib.pyplot as plt
get_ipython().run_line_magic('matplotlib', 'inline')
## Loads the .csv files as matrices
R=np.loadtxt(open("3E16HeOnlyRadius.csv"), delimiter=",", skiprows=1)
H=np.loadtxt(open("3E16FEHeRadius.csv"), delimiter=",", skiprows=1)
##Sets up the desired target depth and bin width for the analysis
binedges=np.linspace(0,150,50)
bincenters=binedges-1.5
## Finds N bubbles per bin and gets the weighted average x and x^2 for
## standard deviation calculation
Rcounts,Redges=np.histogram(R[:,3],bins=50,range=(0,150))
Rsy,_=np.histogram(R[:,3],bins=50,range=(0,150), weights=R[:,1])
Rsy2,_=np.histogram(R[:,3],bins=50,range=(0,150), weights=R[:,1]*R[:,1])
Hcounts,Hedges=np.histogram(H[:,3],bins=50,range=(0,150))
Hsy,_=np.histogram(H[:,3],bins=50,range=(0,150), weights=H[:,1])
Hsy2,_=np.histogram(H[:,3],bins=50,range=(0,150), weights=H[:,1]*H[:,1])
## Tracks the bin index each bubble was placed in and
## appends it the the .csv file, then saves the file as a new name
Rbins=np.digitize(R[:,3], bins=np.linspace(0,150,50))[np.newaxis]
Rbins=Rbins.T
Hbins=np.digitize(H[:,3], bins=np.linspace(0,150,50))[np.newaxis]
Hbins=Hbins.T
R = np.hstack((R,Rbins))
H = np.hstack((H,Hbins))
np.savetxt("3E16HeOnlyRadiusBinned.csv", R, delimiter=",")
np.savetxt("3E16FEHeRadiusBinned.csv", R, delimiter=",")
## Plots the radius of each bubble against the depth of the bubble center in each target
plt.scatter(R[:,3],R[:,1], color='black', marker='o',label='3E16 He only')
plt.xlabel(r'Target Depth (nm)')
plt.ylabel(r'Bubble Radius (nm)')
plt.legend()
plt.savefig('3E16HeScatter', bbox_inches='tight', dpi=1000)
plt.show()
plt.scatter(H[:,3],H[:,1], color='black', marker='o',label='3E16 Fe+He')
plt.xlabel(r'Target Depth (nm)')
plt.ylabel(r'Bubble Radius (nm)')
plt.legend()
plt.savefig('3E16FeHeScatter', bbox_inches='tight', dpi=1000)
plt.show()
```

```

## Plots the concentration of bubble centers per bin
plt.hist([R[:,3],H[:,3]], bins=50, color = ['blue','red']
,edgecolor = 'black', histtype='stepfilled',label=['3E16 He only','3E16 Fe+He'])
plt.xlabel(r'Target Depth (nm), Bin Width = 3 nm')
plt.ylabel(r'Bubble Concentration')
plt.legend()
plt.savefig('3E16CompHist', bbox_inches='tight', dpi=1000)
plt.show()
## Generates the variance of average bubble radius in each bin
Rrad_means, bin_edges, bin_number = stats.binned_statistic(R[:,3],R[:,1], bins=50, range=(0,150))
Rrad_means=np.nan_to_num(Rrad_means)
Hrad_means, bin_edges, bin_number = stats.binned_statistic(H[:,3],H[:,1], bins=50, range=(0,150))
Hrad_means=np.nan_to_num(Hrad_means)
## Generates the standard deviation of average bubble radius in each bin
Rstd=np.sqrt(Rsy2/Rcounts - Rrad_means*Rrad_means)
Hstd=np.sqrt(Hsy2/Hcounts - Hrad_means*Hrad_means)
## Plots the average bubble radius with st. dev. error bars per bin per sample
plt.plot(bincenters,Hrad_means,linewidth=1,marker='^'
,markerfacecolor='red',color='black',label='3E16 Fe+He')
plt.plot(bincenters,Rrad_means,linewidth=1,marker='s'
,markerfacecolor='blue',color='black',ls='--',label='3E16 He only')
plt.errorbar(bincenters,Rrad_means, yerr=Rstd, fmt='blue',ls='none')
plt.errorbar(bincenters,Hrad_means, yerr=Hstd, fmt='red',ls='none')
plt.xlabel(r'Target Depth (nm), Bin Width = 3 nm')
plt.ylabel(r'Average Bubble Radius (nm)')
plt.legend()
plt.savefig('3E16CompAverage', bbox_inches='tight', dpi=1000)
plt.show()

```